UiT
THE ARCTIC
UNIVERSITY
OF NORWAY

Department of Physics and Technology

“Detection of Avalanche Debris Fields in High Resolution SAR Imagery”

—

Erlend Vognild

Master thesis in Energy, Climate and Enviroment EOM-3901 — June 2014

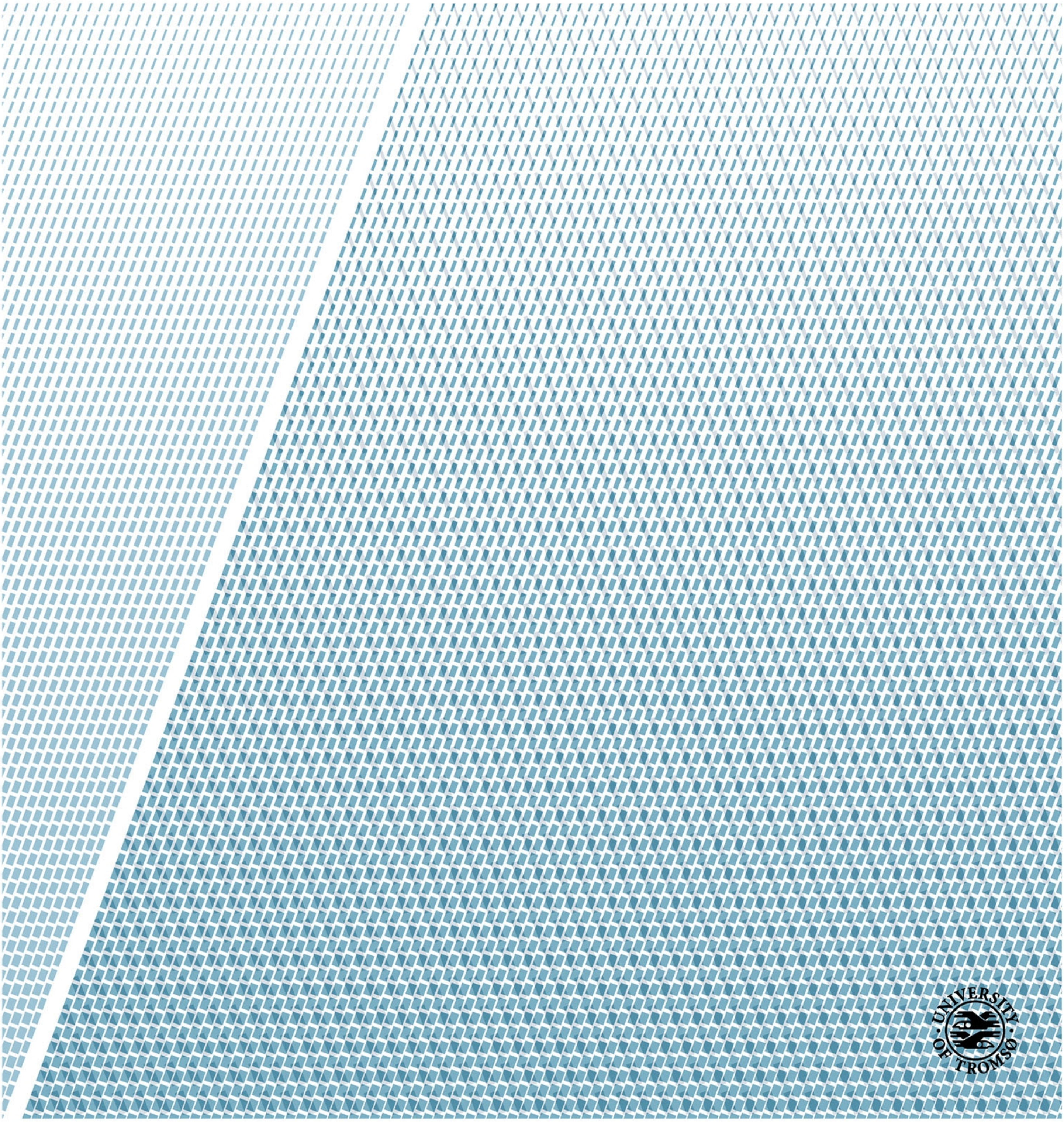

"Detection of avalanche debris fields in High Resolution SAR Imagery"

Erlend Vognild

June 2, 2014

Abstract

During the winter of 2013, Northern Norway saw several large avalanche episodes that caused closed roads and loss of human lives. On Senja and Kvaløya two large avalanches were reported and images from RADARSAT-2 were ordered in ultrafine mode with the goal of detecting these large avalanches in SAR images. Later that year another two images were ordered from RADARSAT-2 that were be used as reference images.

In this thesis an algorithm for automated detection of avalanches is created and applied to the SAR images from the two islands of Senja and Kvaløya. This algorithm trains on several possible debris fields before the best average threshold, moving window size and filter is applied to the full SAR image and an avalanche mask is created. To further remove areas that have a low likelihood of avalanche debris fields, such as lakes and very steep slopes, a slope mask is created from a Digital Elevation Model and added to the avalanche mask.

In the final results several new avalanche debris fields are discovered and verified by applying the DEM to create 3D images, and identifying surrounding terrain as probable for the occurrence of avalanches. The sites that were first chosen as possible avalanche debris fields, are still visible in the final image when average variables have been used in the filtering and thresholding process of the full SAR images.

Acknowledgements

I would like to thank my main supervisor Eirik Malnes for great advice and discussions during my work with this thesis and my co-supervisor Camilla Brekke for guidance and discussion.

My sister Ranghild Vognild for proofreading my thesis and my girlfriend Julianne Othelie Andersen Berge for putting up with many late nights and late dinners.

A final thank you to my fellow master students at Norut brakka for good discussions and for keeping a good mood throughout out the last semester at the University of Tromsø.

Contents

List of Figures

Chapter 1

Introduction

Norway is a country with vast mountainous areas, some of which are avalanche prone. Much Norwegian infrastructure is located in or near such areas, and each year avalanches take lives and damage infrastructure. During the winter of 2013, 8 persons were killed and several roads were closed during the avalanche season. Infrastructure is affected by avalanches by either destruction of buildings or closure of roads and rail roads due to avalanches blocking the roads and rail roads or the danger for avalanches deemed to high. In this thesis an algorithm is developed that will automatically detect avalanche debris field from SAR images.

For tourist travelling the mountains of Norway there are several tools available to help predict the avalanche danger for the local area where they are planing their hikes. One tool is the newly created website Varsom.no. Varsom is a project started by Norwegian Water Resources and Energy Directorate (NVE) in cooperation with Jernbaneverket, Statens Vegvesen og Meterologisk institutt. Varsom.no have daily updates on dangers of not only avalanches, but also floods and landslides. These events are thought to increase in frequency in the following years due to more extreme weather and global warming and avalanches are expected to be especially affected by weather changes.

Measures to protect infrastructure from avalanches are securing it with avalanche walls, which can be described as large dirt walls as seen in Figure 1.1. These are built to direct the avalanche away from infrastructure, especially around roads and rail roads. Avalanche fences are built in avalanche prone slopes, as seen in Figure 1.2 above residences in Hammerfest, and avalanches might be manually released before they become large enough to reach and damage infrastructure.

To locate and forecast avalanche danger, Varsom.no have employed several persons that observe and register weather and snow conditions in mountainous areas. This allows for an avalanche danger map to be constructed and people who enters these high risk areas can check the avalanche danger before venturing there. This is however very restricted to the areas where observers are located, and does not cover the entirety of Norway's mountainous regions. It is also dependent on timing as an avalanche can occur during a heavy snowfall just to be covered by snow by the time an observer reaches the area.

Figure 1.1: Avalanche fences installed above residences to stop avalanches from happening in Hammerfest, Finnmark. Foto: Statens Vegvesen

Figure 1.2: A large avalanche released by Staten Vegvesen is stopped by two avalanche meadows in Lavangsdalen, Troms. Foto: Statens Vegvesen

A tool that might help in giving a far better coverage and a higher frequency for observation is remote sensing. Remote sensing from satellites are today used to monitor deforestation, detect change in sea ice and land ice, surveillance of coast lines, detection of oil spills, floods, damages after storms and monitoring of snow cover to mention a few [Storvold et al., 2005], [Frauenfelder et al., 2010] and [Shirvany et al., 2012]. But detection and monitoring of avalanches with Synthetic Aperture Radar (SAR) have not been researched much, and therefore only a few research papers have been published.

In [Bühler et al., 2009] an optical sensor were mounted on a plane and used to locate and automatically classify several avalanches in a test site in Davos, Switzerland. They created an algorithm that could detect and classify large scale avalanche events, and medium to small avalanche debris fields. They did, on the other hand, meet some restrictions with bad weather, and false classifications due to rough surfaces as wind snow pack and sparsely vegetated areas[Bühler et al., 2009]. In [Larsen et al., 2010] they also had good results when classifying avalanche deposits with optical sensors, but here they also concluded that illumination and weather was challenging for optical sensors.

Spaceborne SAR sensors have several great advantages compared to optical sensors. Weather and clouds are not an issue for SAR, and it is not dependent on an external source for illumination. This makes the SAR sensor useful under any weather condition and time of day. New SAR sensors, RADARSAT-2 (RS-2), Cosmo Skymed and TerraSAR-X to mention a few have the high resolutions that is required for detection of avalanche debris fields[Bühler et al., 2009]. They will be able to detect avalanche debris fields that are located underneath a new layer of fresh dry snow as C-band radar penetrate unperturbed snow, which is something that prove problematic for optical sensors [Frauenfelder et al., 2010]. In [Wiesmann et al., 2001] SAR images were used to create a RGB image where each channel in the image were represented by an image taken with several weeks between them, but from the same location of the sensor. Here they showed that an avalanche did indeed show on the RGB image, and were able to verify their finding with both aerial imagery and manual mapping done by the Swiss Federal Institute for Snow and Avalanche Research.

In [Malnes et al., 2013] data from RS-2 was ordered after two large avalanches on Senja and Kvaløya in april 2013. Here a difference in backscatter were measured from inside and outside the avalanche.

This thesis applies the same data from RS-2 that were used in [Malnes et al., 2013], as well as a set of reference images and a Digital Elevation Model, and an algorithm for automated detection of avalanche debris fields is developed.

1.1 Objective

The objective of this thesis is to construct a new, automated method for locating avalanche debris fields on high resolution SAR imagery.

1.2 Contribution

A method for detecting and finding avalanche debris fields has been developed and is showing promising results. When the key features, found by the filtering algorithm, are applied to the RS-2 images provided by Norut, several new avalanche sites are discovered,and their surrounding topography is verified to be of such nature that it would be natural to assume an avalanche debris field can be found there. A trained eye can spot the avalanche debris fields by looking at the terrain surrounding the relative high backscatter area. This data can be used to count avalanches over huge areas without the need of observers in the field, that can help creating avalanche runout models for mountains areas or uploaded to avalanche forecast websites and added to maps that are available to the public. With a higher temporal resolution of images, this data can be used to find the repetition time of avalanches as it would be possible to watch avalanches over a longer period of time.

1.3 Outline

Chapter 2: Investigation of avalanche theory and the meteorology in the time before and after the images were taken. The avalanche theory contains earlier research done on avalanche runout zones, and density of the snowpack found in avalanche debris fields depending on the avalanche type.

Chapter 3: A closer look on spaceborne SAR geometry is reviewed. Geometric distortions caused by the geometry are studied in detail as well as the resolutions of a SAR system and geocoding of the SAR image. Speckle and how it occurs on SAR images is investigated. Also how to remove the speckle with 4 well known speckle reducing filters. These filters are Median, Mean, Frost and Lee filters, and their advantages and disadvantages are reviewed.

Chapter 4: Theory regarding scattering reviewed. In detail scattering theory on dry snow and wet snow and how water in the soil effects the backscatter. Also how forests affect backscatter, with or with out leaves.

Chapter 5: Review of the data available for this thesis. Two images containing avalanches from Senja and Kvaløya, and two reference images, a Digital Elevation Model and geometric aberration mask for each of the 4 SAR images. The filtering algorithm used to find the best filter, threshold and best size of the moving window is described in detail. The slope algorithm that is used to remove areas found too steep or flat will also be described before finally describing the final algorithm that use data found earlier to automatically detect avalanche debris fields on entire SAR images.

Chapter 6: Results and discussion; Creating RGB images and visually locating avalanches that are used to create subsets, before manually drawing avalanche masks for each subset. Results from a filtering algorithm are reviewed by observing the performance of each filter with different thresholds and moving window sizes, and comparing these results with the manually drawn avalanche mask for each of the subsets. Applying the slope mask and discussing the new avalanches found after filtering and thresholding the complete images over Senja and Kvaløya. Discussing possible errors in the algorithms and what can be done to improve the algorithms will also be reviewed.

Chapter 7: In the conclusion the final thoughts and ideas for how future work should be aimed is discussed.

Chapter 2

Snow and weather theory

Weather plays the most important role in creating the conditions that are needed for avalanches to occur, and one of the safest signs of avalanche danger is if there have been movement of snow. Snow movement can be performed by either wind or snowfall, and avalanches danger rises the more snow is moved. Change in temperature can cause weak layers in the snow to collapse and avalanches to be released. A common factor for all avalancehs are that they are released in areas with a slopeof more than 30°, [Landrø, 2002].

2.1 Avalanche theory

Avalanche debris fields can be found randomly along the avalanche path, but the size and amount of the deposits are dependent on the features of the ground where the avalanche move. For example a debris field might be left in a small depression along the path of the avalanche, but most part the main debris field will be deposited where the avalanche come to a final stop.

The characteristic of the surface of the debris field is dependent the hardness of the snow, distance travelled and the amount of water in the snow. Generally an avalanche debris field is more broken up the further the avalanche has travelled. But common for them all is that there is an increase in density in the debris field compared to the surrounding unperturbed snow. A general debris field density can be seen in table 2.1 [McClung and Schaerer, 2006].

Type of avalanche	**Density**
Small dry avalanche	200kg/m^3
Medium to large dry avalanche	300-400 kg/m^3
Wet avalanche	500-600 kg/m^3
High-speed dry avalanche	500 kg/m^3
Slush flow	up to 1000 kg/m^3

Table 2.1: Typical debris fielddensities of snow in avalanche debris fields [McClung and Schaerer, 2006]

The density changes with the type of avalanche. Small avalanches of hard slab snow may have very little change in density if the avalanche travels a only a short path, whereas for larger, high speed avalanches of dry snow the density might double.

In [McClung and Schaerer, 2006] it is shown that the density also increase with the depth of the deposit. Smaller snow particles nearer the bottom of the avalanche is easier to pack and less air is found amongst the particles. In [Dent et al., 1998] they also measured density in a moving avalanche where they measured the density near the bottom of the avalanche flow to $350kg/m^3$ down to an average of about $250kg/m^3$ in the top of the flow [Dent et al., 1998].

Avalanche runout distance

The furthest point the avalanche moves is called the the runout distance. This distance is dependent on several factors. The steepness of the slope, wetness of the snow, difference in height, friction between the avalanche and the surface where it slides. According to [McClung and Schaerer, 2006] the runout distance is best determined by:

1. Long term observation of avalanche paths
2. Observation of damage to vegetation, ground or structures
3. Search historical records, as old newspapers, to find information of old avalanche paths.

This is very time consuming and expensive as observers or cameras need to be installed in all regions of interest to document every avalanche path. But this method is considered more accurate compared with dynamic models as these model contain risky assumptions as the friction between the avalanche and the ground [McClung and Schaerer, 2006]. In areas where no such data exists, empirical models can be used. One empirical approach is to measure at least 30 runout distances from a mountain range and calculating the extreme runout distance based on these distances. This method is not considered to be accurate enough for many applications, but the uncertainty can be specified in statistical terms by giving a probability for an avalanche runout, based on certain terrain criteria from the avalanche path[McClung and Schaerer, 2006]. The large avalanche on Kattfjordeidet, Kvaløya, can be seen in Figure 2.1, and the runout zone can be identified far out onto the frozen lake.

2.2 Meteorology

Meterology is the main contributor to avalanches as they occur only after changes in weather and movement of snow. Large snowfalls will give an increased avalanche danger, wind will move snow from one area to another creating avalanche danger where the snow is deposited, and change in temperature can cause weak layers in the snow to collapse and release avalanches [Landrø, 2002].

Figure 2.1: A large avalanche on Kattfjordeidet, the runout zone can be seen to stretch far onto a frozen lake. Foto: storm.no

The days before the avalanches the two large avalanches on Senja and Kveløya, Northern Norway had experience a large amount of snow together with strong winds. Data from eklima.no from the end of February, from the weather station on Langnes, shows that there was a warm period of about 6 days with a daily mean temperatures above 0°C. Followed by March with a mean temperatures below 0°C, Figure 2.3. This is thought to have created the weak layers found in Tromdalen during NGI's examination of the snow layers, and it is also mentioned as a probable cause for the avalanches in [Malnes et al., 2013]. In the days before the 2 avalanches, Northern Norway experienced strong winds with a daily mean of up to 9m/s together with a lot of perception and an increase in snowdepth from 20cm to 50 cm in the last week of March, Figure 2.2, which caused snow build-up on the icy layers found in [Brattlien, 2013]

In the days before the reference images, σ_r, were taken the weather for Senja and Kvaløya changed. In Figure 2.4 it can be observed that in the days before the image over Senja was ordered on the 27th there was relatively small amounts of precipitation compared with the days when the image of Kvaløya was taken on the 29th. This means the the soil was saturated with moisture at the time of the reference image from Kvaløya, and not as moist on Senja.

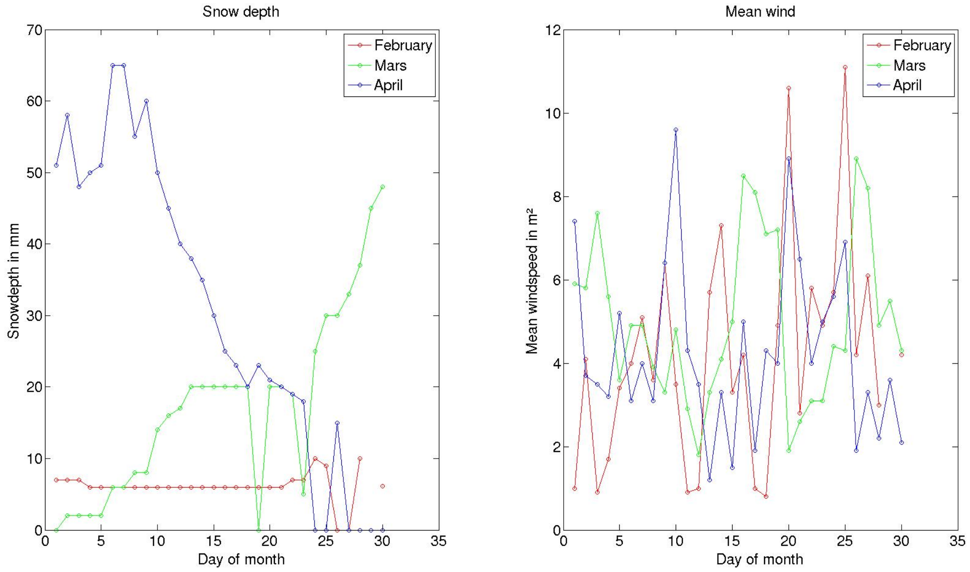

Figure 2.2: Snow depth and mean wind for February, March and April from the weather station on Langnes, Tromsø. Data from www.eklima.no

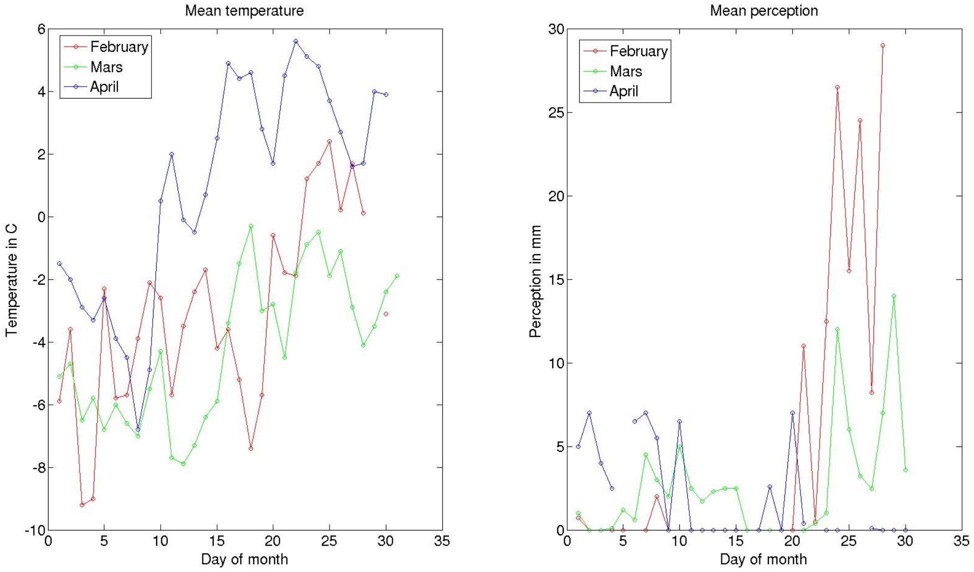

Figure 2.3: Mean temperature in C and mean perception for February, March and April from the weather station on Lagnes, Tromsø. Data from eklima.no

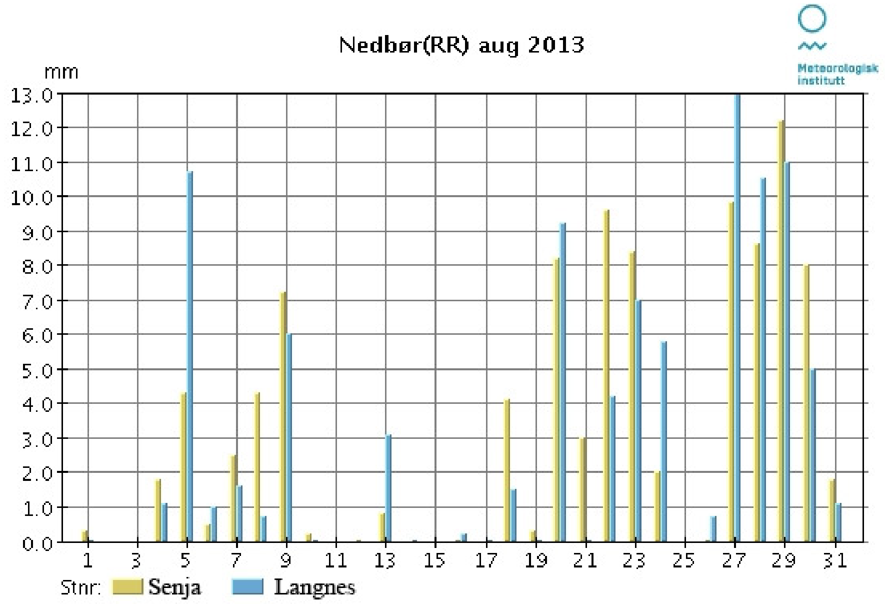

Figure 2.4: Precipitation on Senja and Langnes August 2013, Tromsø. Data from www.eklima.no

Chapter 3

Synthetic Aperture Radar imaging

Synthetic Aperture Radar(SAR) is very well suited for a wide range of application, and especially in sea and ice monitoring[Wakabayashi et al., 2013], oil pollution monitoring[Cheng et al., 2011], snow monitoring [Pivot, 2012] and to a small extent, detection of avalanche debris fields[Malnes et al., 2013]. A SAR sensor can penetrate cloud cover and is not dependent on an external source for illumination as it is an active sensor that provides its own. This makes the SAR sensor very suitable for use in the Northern hemisphere during the winter, due to few hours of sunlight during the days and often clouds cover the country. Due to the nature of SAR geometry several geometric aberrations can be found in SAR images that have to be corrected for. These aberrations will be reviewed in this chapter, together with the geometry of a spaceborne SAR. Resolution for SAR systems and how they depend on the bandwidth and frequency will be reviewed. Speckle is also a part of SAR images, and it will be reviewed together with techniques of how to remove it.

3.1 The radar equation

The radar equation describes the relationship between the transmitted power and the received backscatter. This can be calculated with the radar equation:

$$\begin{aligned} P_r &= \frac{P_t G^2 \lambda \sigma}{(4\pi)^3 R^4} \\ &\text{where} \\ P_r &= \text{Power received at the antenna} \\ P_t &= \text{Power transmitted by the antenna} \\ G &= \text{Antennae gain} \\ R &= \text{Distance between antenna and target} \\ \lambda &= \text{Operating wavelength} \\ \sigma &= \text{Radar target cross section} \end{aligned} \tag{3.1}$$

The signal received is often contaminated by noise produced by the antenna itself or atmospheric propagation. By lookig at the signal recieved at the antenna and the noise a Signal to Noise Ration(SNR) can be created.

$$SNR = \frac{S}{N_0} = \frac{P_t G^2 \lambda^2 \sigma}{(4\pi)^3 R^4 N_0} \tag{3.2}$$

As long as the SNR is larger than 1, the sensor is capable for separating the signal from the noise. But if the SNR is lower than 1 the sensor can no longer separate the signals from the noise.

3.2 Physical geometry of SAR systems

A SAR sensor is spaceborne or airborne, either mounted on a unmanned aerial vehicle (UAV), or launched into space. This gives the sensor a geometry that has to be understood to be able to correct for possible geometric aberrations in the images. In Figure 3.1 the basic geometry of a spaceborne sensor is laid out. The direction the sensor is moving is called the azimuth direction. The distance from the sensor to the target in the direction perpendicular on the azimuth direction is called the range direction. As seen in Figure 3.2b the range direction points from the point N towards F. The distance between N and F is know as the swath width [Oliver and Quegan, 2004]. The distance from P to X is called the slant range and is denoted R_θ.

Due to the height of spaceborne SAR's the curvature of the earth has be taken into account when creating the image, as can be seen in Figure 3.2b. The radar beam is covering a curved range distance which will affect the output. All the parts in Figure 3.2a can be described as:

$$R_\theta = [R_E + h]\frac{sin[\gamma]}{sin[\theta]} \tag{3.3}$$

$$R_\theta^2 = R_E^2 + [R_E + h]^2 - 2R_E[R_E + h]cos[\gamma] \tag{3.4}$$

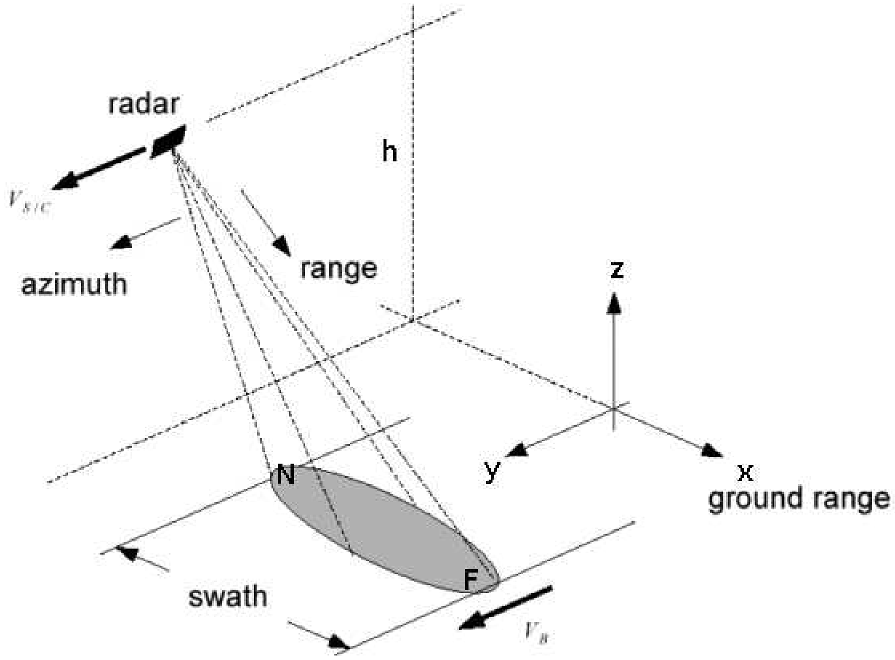

Figure 3.1: Illustration of the basic geometries for a SAR. Image: foto.hut.fi

$$R_g = R_E * \gamma \tag{3.5}$$

$$\gamma = \theta - \alpha \tag{3.6}$$

$$sin[\alpha] = \frac{R_E}{R_E + h} sin[\theta] \tag{3.7}$$

The variables in equation 3.3 - 3.7 are represented in Figure 3.2a. For a airborne sensor, $R_E \gg h$, so eq. 3.3 and eq. 3.4 is reduced to a flat earth approximation and the equations made considerably easier. For spaceborne sensors some approximations can be made, if γ is very small this can be approximated, $sin[\gamma] = \gamma$.

Figure 3.2b shows how the beam from the reader is spread out on the curvature of the earth and eq. 3.8 shows the time delay from a point with a distance of R_θ from the sensor. The duration of the radar pulse is seen as $c\tau_p$ on Figure 3.2b.

$$\tau = 2R_\theta / c \tag{3.8}$$

A scatterer that is located R_θ from the sensor returns a pulse with length $c\tau_p$ with a time delay as described in eq. 3.8. In the range direction a SAR can use both ground range and slant range data. But when using the slant range data, the data will have to be corrected for since each pixel is represented as how the

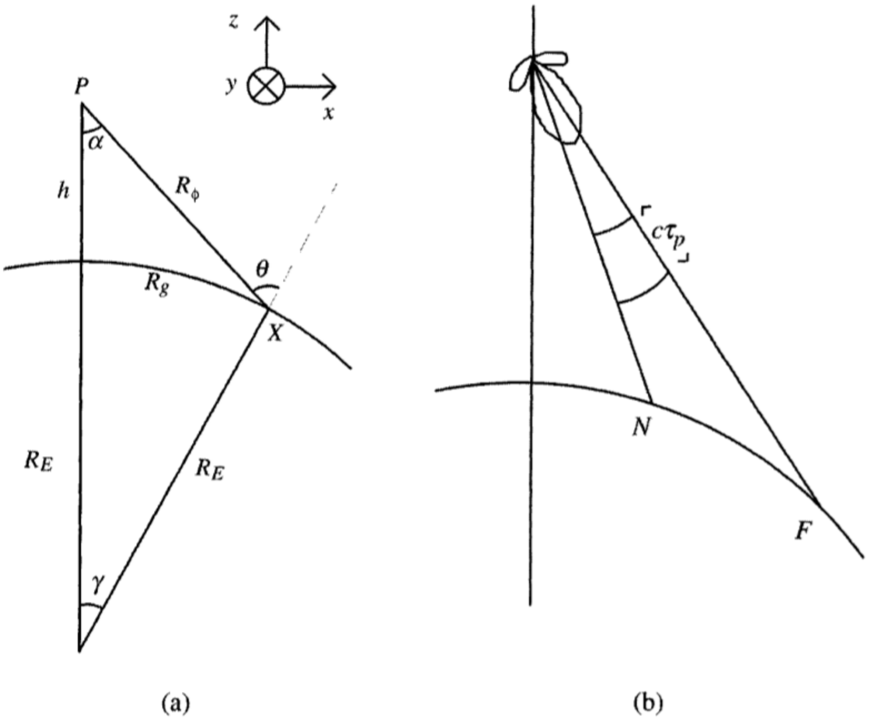

Figure 3.2: Figure (a) Illustration of the geometry of a SAR sensor. Figure (b) Illustration of the beam from a radar [Oliver and Quegan, 2004].

SAR actually measures the pixel. This effect is illustrated in Figure 3.3 and can be seen in practise in Figure +refslantimage.

The main principle behind a SAR sensor is that it synthesizes a large antenna by measuring the change in frequency of the signal in the azimuth direction. This change in frequency is called the Doppler effect and allows for SAR sensors to have have a far greater resolution that Real Aperture Radars (RAR) at large heights without the need of enormous antennas. At each point along the azimuth direction the sensor sends out a pulse of length τ, which is backscattered to the antenna over the entire beam footprint. Each separate target in the azimuth direction will have a lightly different angle towards the antenna and the scattered signal from each target will therefore have a slightly different frequency. The SAR imaging systems use this change of frequency and time duration to determine where in the azimuth direction the signal is returned from and by finding the location creating an image [Oliver and Quegan, 2004].

3.3 Resolutions of SAR imaging

The resolution for a SAR sensor can be seperated in to 3 resolutions, the azimuth resolution, range resolution and the spatial resolution. Whereas azimuth and range resolution makes up the spatial resolution. A resolution in a SAR is

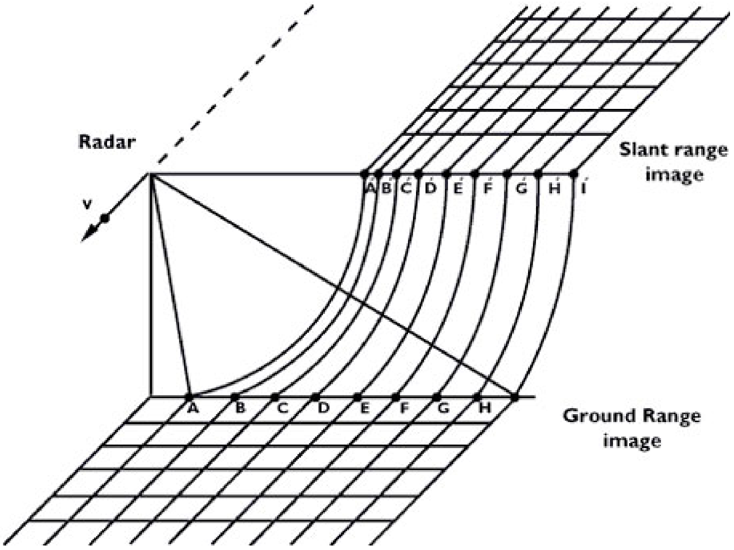

Figure 3.3: Illustration of how pixels with the same size in the range direction get distorted in the slant range direction. Image: ESA

defined as the minimum distance between two point where the points can be separated, [Elachi and Van Zyl, 2006].

Azimuth resolution

The azimuth resolution is in [Elachi and Van Zyl, 2006] given as:

$$X_a = L/2 \tag{3.9}$$

Where L is the length of the antenna.

Range resolution

In [Elachi and Van Zyl, 2006] the ground range resolution is given by

$$X_r = \frac{c}{2Bsin(\theta)} \tag{3.10}$$

Here c the speed of light, θ the incident angle and B the bandwidth.

Spatial resolution

The spatial resolution can be described as the smallest object that can be described on the image and is made of both the azimuth and range resolution.

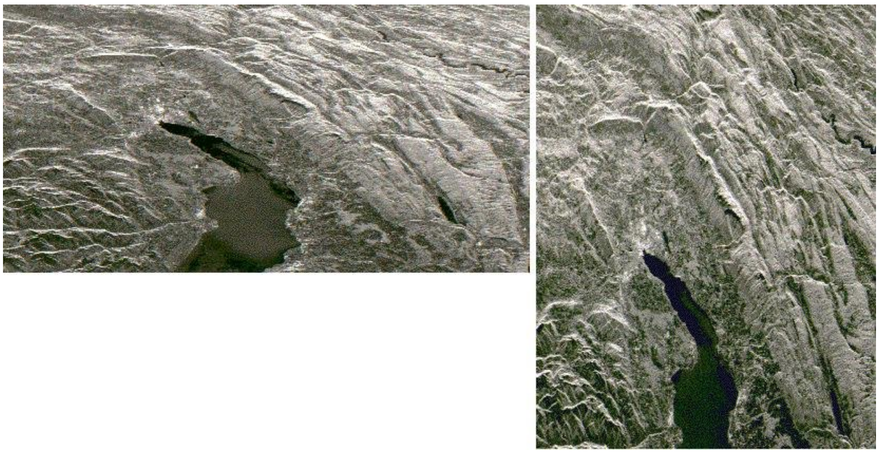

Figure 3.4: The left image shows a slant range image, and the image on the right has been slant range corrected. Image: ESA

3.4 Geometric distortions in SAR images

Due to the sidelooking nature of SAR sensors, several geometric distortions will appear on SAR images. These distortions will have to be corrected for. In Figure 3.4 the slant range image can be seen to the left and the ground image to the right. Other distortions can be called elevation distortions and include slant range correction, foreshortening, layover and shadowing.

3.4.1 Slant range correction

The slant range error occurs as a direct response to the sidelooking nature of SAR sensors, and has to be adjusted for. An unadjusted slant range image can be seen to the left in Figure 3.4 and a corrected image to the right. The correction of this distortions is done by the following equation from [Chuvieco et al., 2009]:

$$Pr = \frac{c\tau_p}{2sin(\theta)} \tag{3.11}$$

where τ_p is the pulse pulse length as seen in Figure 3.2b and θ the incident angle.

3.4.2 Shadowing

Due to the side looking nature of SAR systems large objects will cast shadows behind them as seen in Figure 3.5. This effect will increase with lower incident angle of the satellite.

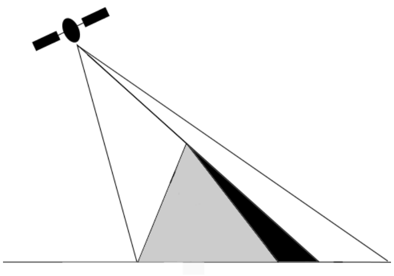

Figure 3.5: Figure illustrating the effects of shadowing, the elevation casts a shadow in the radar foot print.

3.4.3 Foreshortening

Foreshortening happens when a slope in the topography causes a reduction in time between the two signals from the slopes bottom and top. This again causes the two points to appear nearer each other on the image. As seen in Figure 3.6 point b will appear closer to point a the SAR image, compared to the distance between them on the ground.

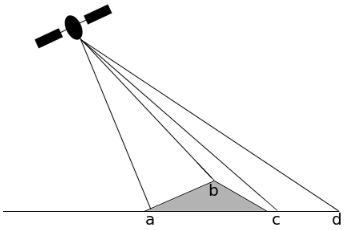

Figure 3.6: Figure illustrating the effects of foreshortening. Point **"b"** appears close to point **"a"** on the SAR image than it is in reality

3.4.4 Layover

This effect occurs when the radar beam reaches a slopeso steep that the signal backscattered from the top of the slope, Point *a* in 3.7 reaches the radar sensor before the signal from the bottom of the slope Point *b* in 3.7. When this happens in the slant direction point *b* is placed in front of point *a* in the SAR image.

3.5 Geocoding

Geocoding is often required and preferred before SAR images can be of good use to the end user. When an image is geocoded each pixel is attuned to a coordinate system that other images taken with different sensors or at different times also are attuned to. This allows for direct comparing of pixels between

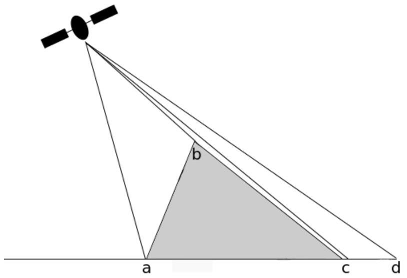

Figure 3.7: In extreme cases of foreshortening point **"b"** will appear in front of point **"a"** on the SAR image. This effect is called layover

images taken with different sensors and of different times. This is especially helpful when looking at changes in images, as when looking at the movement of glaciers, deforestation, change after environmental disasters, or as in this case, detection of avalanche debris fields [Wiesmann et al., 2001].

Today geocoding is performed by a fully automatically algorithm, called GSAR, developed at Norut. This algorithm take advantage of the high precision location of the sensor in its orbit and can therefore geocode the image with high accuracy without the need for a Ground Control Point(GCP). To perform geocoding the first step is to remove geographic aberrations and radiometric distortions as these ambiguities will greatly reduce the end quality of the image. Radiometric distortions include range spreading loss, resolution cell power effects and antenna pattern. Geometric distortions are layover, foreshortening and shadowing [Lauknes and Malnes, 2004]. This distortions are corrected by GSAR.

Information from the DEM is used with the Range Doppler equations to transform from the map to SAR coordinates in range and azimuth directions. The quality is dependent on the accuracy of the SARs orbital location and DEM quality [Lauknes and Malnes, 2004]. The algorithm creates two geocoded images, one is the SAR image, geocoded, and the second in a mask that masks away the geometric distortions mentioned in Section 3.4.

3.6 Speckle

All images from SAR, lasers and other coherent imaging system are affected by speckle. Speckle is apparent and is visible as white and black pixels in the image. Speckle degrades the overall quality and makes the interpretation of the image more complicated. Speckle occurs when the coherent electromagnetic waves from the transmitter reaches an area with many scatterers located in the same resolution cell . This returned wave can be described as

$$Ae^{i\phi} = \sum_{k=1}^{N} A_k e^{i\phi_k} \tag{3.12}$$

where $A = Amplitude$, $Intensity I = A^2$, the real part is $Acos(\phi)$ which is also described as the in-phase component. The complex part is $Asin(\phi)$ which is the quadrature component. The phase is found in ϕ. Eq. 3.12 contain all the scatter data from one resolution cell in the original complex SAR image [Oliver and Quegan, 2004].

When all the scatteres contribute to the backscatter waves with different phase and amplitudes speckle is created. From eq 3.12 it can be seen that the signal received at the sensor is very much affected by the interference created by the difference in phase among the scatterers [Oliver and Quegan, 2004].

3.7 Speckle reduction

The process of removing speckle can generally be separated into two stages; multilooking, which is usually performed before acquiring the image or during geocoding (with the GSAR software), and filtering which is performed in the post processing of the image [Mansourpour et al., 2006]. Filters can be applied to remove speckle and to enhance contrast in such a way that interpretation of the image becomes easier and wanted information becomes clearer for the viewer. There are many filtering techniques and algorithms that can be applied to SAR images. In this thesis the focus is on filters that have been tested to work well with SAR images and speckle removal in earlier research [Gagnon and Jouan, 1997] and [Mansourpour et al., 2006].

3.7.1 Multilooking

In most cases, speckle is an effect the user want to remove from the image, and this depends on what part of the image the user is looking. In a Singel Look Complex (SLC) image, multilooking as always performed, whereas a Ground Range Detected(GRD) image are images that have been corrected for slant range error and multilooked. Multi-looking is often the first step when reducing speckle from a SAR image. Multi-looking reduces speckle by splitting the radar beam into several narrower beams. Each beam will perform a look over the same area and an average for each pixel is calculated to reduce the amount of speckle. This could also be seen as a Box filter or mean filter as it calculates the mean and averages out the speckle. This does on the other hand also degrade the resolution of the image.

3.7.2 Lee Sigma Filter

The Lee Sigma filter is based on the statistical distribution, Gaussian distribution, of the numerical value of each pixel inside the moving window. A two sigma probability is described as the probability that a random variable is within 2 standard deviation of the mean. And the probability for a random variable to be within the two standard deviation is 0,955 for a one dimensional Gaussian distribution. [Lee, 1983] In the smoothing process, any pixel outside of this two sigma range is considered to be something outside of the population and is not taken into account when the average is calculated. The way the Lee filter calculates a new value for the central picture is by

$$Value_{out} = Mean + K(Value_{in} - Mean) \tag{3.13}$$

where "Mean" is the mean of all pixels in the moving window, *Value in* and *value out* are the values of the central pixel after and before the calculation. K is calculated by

$$K = Var(x)/[Mean^2 * \sigma^2 + Var(x)] \tag{3.14}$$

and the variance for the central pixel var(x) is

$$Var(x) = \frac{(Variance_W) + (Mean_W)^2}{(\sigma^2 + 1)} - Mean_W^2 \tag{3.15}$$

3.7.3 Average filter

The average filter is very straight forward. A moving window sets the boundaries for in which the filter works inside. The moving window is moved one pixel at the time, meaning that the central pixel of interest is always moved one pixel to the side. The new value, or output value, of the pixel of interest is calculated by taking the average of the entire moving window and replacing the pixel of interest with the average. This gives a filter which removes speckle by averaging it and blurs details and edges. The mean filter works well if details and edge preservation is not important, but removing of speckle and small clusters of speckle like noise [Huang and van Genderen, 1996].

3.7.4 Median filter

The median filter is also a very straight forward filter that works in the same way as the average filter, but instead of finding the average it calculates the median. It removes pixels with big spikes in value. Random distributed pixels with high or low value of less than half of the moving windows width are replaced, whereas pulse functions and unit step functions that are larger than half of the moving window are not touched. This allows for removal of speckle, while edges and details large enough will remain. [Mansourpour et al., 2006]

3.7.5 Frost filter

The Frost filter was developed in 1982 as SAR images became more available and the need for statistical models for radar speckle became more apparent. Frost et al made a filtering model specifically designed for microwave sensors and a model that treats speckle as a multiplicative noise [Frost et al., 1982]. It is well used and studied in other papers [Mansourpour et al., 2006] and [Gagnon and Jouan, 1997] about speckle removal, while maintaining resolution, edges and details in SAR images. Here the central pixel is replaced with a weighted sum of the values in the moving window, neighbouring pixels are weighted higher than pixel further away. Also the weighting factor are increased when the variance inside the moving window increase. The formula for the filter is:

$$
\begin{aligned}
DN &= \sum_{nxn} k\alpha e^{-\alpha|t|} \\
\text{where} & \\
\alpha &= [4/n\overline{\sigma}^2][\sigma^2/\overline{I}^2] \\
k &= \text{normalization constant} \\
\overline{I} &= \text{local mean} \\
\sigma &= \text{local variance} \\
\overline{\sigma} &= imagecoefficientofvariationvalue \\
|t| &= |X - X_0| + |Y - Y_0|\text{and} \\
n &= \text{size of the moving window}
\end{aligned}
\tag{3.16}
$$

This makes for an excellent filter for reduction of speckle and maintaining details and edges in the SAR images [Shi and Fung, 1994] and [Gagnon and Jouan, 1997]

3.8 Thresholding

Thresholding can be used to classify part of SAR images when two images of the same site exists. If one image has a higher backscatter in one small location in the first image, for example avalanche debris fields, this area will be easier to classify when subtracting the σ_r image. This allows for setting up a threshold where the pixel are either classified as inside the high backscatter area, or outside of it. In [Moser and Serpico, 2006] this method is used to detect change in SAR images. One factor that affects the threshold is moisture in the ground when the reference image is taken. If the moisture is high per volume unit the backscatter is expected to be lower, whereas if the ground is dry it will be higher. When calculating the threshold for one area this is not a problem, as the soil wetness is homogeneously distributed in the SAR image, but when comparing images from different locations, taken at different times, the difference in soil wetness will have an effect on the threshold for that given region. + After $\Delta\sigma$ has been calculated from $\sigma_a - \sigma_r$ the threshold a threshold is tested. Figure 3.8 shows an example of how the $\Delta\sigma$ image is created and what it looks like after the subtraction. An avalanche can be seen as a stronger backscatter signal in the left matrix in Figure 3.8 that represents σ_a, the homogeneous reference image, σ_r is subtracted, and the final product $\Delta\sigma$. The $\Delta\sigma$ image is the image where the avalanche pixels are classified by testing thresholds from -1 to 3.

For Figure 3.8 it can be noticed that the threshold would have to be between 0 and 1 for the avalanche pixels to be separated from the surrounding.

In Figure 3.9 the reference image,σ_r, gives a 1dB weaker backscatter than in Figure 3.8. Here the threshold would have to be within 1 and 2 for the avalanche to be separated from the surroundings. This means that a threshold found to be working for one area might not be the best threshold for another. Especially

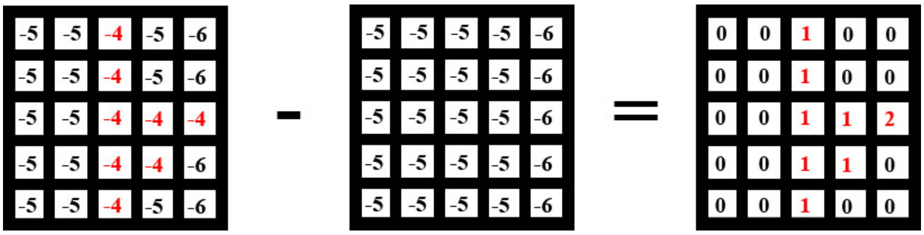

-5	-5	-4	-5	-6		-5	-5	-5	-5	-6		0	0	1	0	0
-5	-5	-4	-5	-6		-5	-5	-5	-5	-6		0	0	1	0	0
-5	-5	-4	-4	-4	-	-5	-5	-5	-5	-6	=	0	0	1	1	2
-5	-5	-4	-4	-6		-5	-5	-5	-5	-6		0	0	1	1	0
-5	-5	-4	-5	-6		-5	-5	-5	-5	-6		0	0	1	0	0

Figure 3.8: $\sigma_a - \sigma_r = \Delta\sigma$ The avalanche in σ_a and $\Delta\sigma$ are represented with red numbers. This is a example of how the avalanche debris field has a higher backscatter than the surrounding area and the reference image. The threshold is between 0 and 1

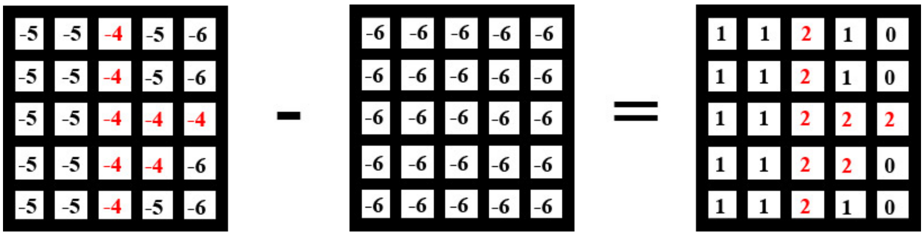

-5	-5	-4	-5	-6		-6	-6	-6	-6	-6		1	1	2	1	0
-5	-5	-4	-5	-6		-6	-6	-6	-6	-6		1	1	2	1	0
-5	-5	-4	-4	-4	-	-6	-6	-6	-6	-6	=	1	1	2	2	2
-5	-5	-4	-4	-6		-6	-6	-6	-6	-6		1	1	2	2	0
-5	-5	-4	-5	-6		-6	-6	-6	-6	-6		1	1	2	1	0

Figure 3.9: $\sigma_a - \sigma_r = \Delta\sigma$ The avalanche in σ_a and $\Delta\sigma$ are represented with red numbers. Here the ground in the reference image σ_r is wet and gives a general lower backscatter than the winter image. The threshold is between 1 and 2

if the reference image σ_r is taken at a different time and one of them after heavy rain while the other is after a dry period. In [Susan Moran et al., 2000] a difference of 3dB have been observed in the same area before and after a 25% increase of moisture in the soil where there were no vegetation. While in [Kasischke et al., 2009] they conclude with that C-band radar has the potential to detect change backscatter based on change in soil moisture.

A third case that can occur is when a negative threshold is found. This can be caused by the area surrounding the avalanche having a very weak backscatter, while the avalanche have a relative high backscatter compared to its surrounding. This case can be seen in Figure 3.10 where the threshold is expected to be between 0 and -1. The reason for such scenario can be due to wet snow

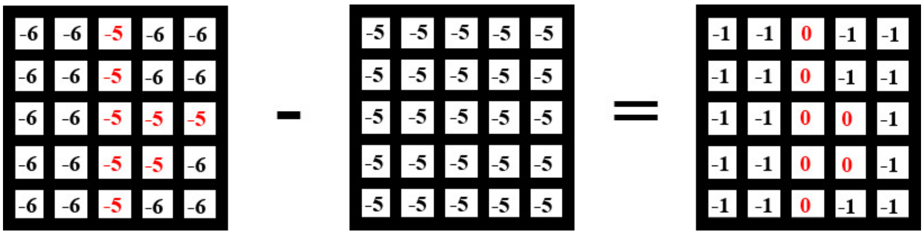

-6	-6	-5	-6	-6		-5	-5	-5	-5	-5		-1	-1	0	-1	-1
-6	-6	-5	-6	-6		-5	-5	-5	-5	-5		-1	-1	0	-1	-1
-6	-6	-5	-5	-5	-	-5	-5	-5	-5	-5	=	-1	-1	0	0	-1
-6	-6	-5	-5	-6		-5	-5	-5	-5	-5		-1	-1	0	0	-1
-6	-6	-5	-6	-6		-5	-5	-5	-5	-5		-1	-1	0	-1	-1

Figure 3.10: $\sigma_a - \sigma_r = \Delta\sigma$ The avalanche in σ_a and $\Delta\sigma$ are represented with red numbers. Here σ_a has a lower backscatter then σ_r which cause the threshold to be between -1 and 0.

surrounding the avalanche deposit. The higher backscatter from the avalanche can be caused by either the avalanche consists of dry snow transported from higher altitudes that were deposited there a short while before the image was taken, or the increase in backscatter is caused by increased roughness in the avalanche debris field compared to the surroundings.

Chapter 4

Scattering theory

In this chapter theories surrounding scattering of electromagnetic waves will be introduced. The scattering from snow covered ground depends on the wetness of the snow, particle size, density surface roughness[Guneriussen et al., 1999]. All of which undergoes a change during an avalanche. Scattering from forests will be reviewed, both with and without leaves.

4.1 Scattering of electromagnetic waves in snow

Active microwave sensors have seen an increase in use in the field of detection of snow covered surfaces, retrieval of snow covered areas in mountainous regions [Storvold et al., 2005], retrieval of wet snow [Nagler and Rott, 2000], monitoring of snow melt [Koskinen et al., 1997] and detection of avalanche debris [Malnes et al., 2013] amongst other.

C-band SAR sensors have the ability to penetrate approximately 10m of dry snow at densities of $0.2gcm^3$. The dielectric constant for dry snow is very low so in the air/snow boundary very little of the electromagnetic wave is reflected as surface scattering but most of it is transmitted into the volume pack of the snow and scattered at the snow/ground boundary instead. In Figure 4.2 the change in penetration depth of the snow and how it depends on the density of the snowpack and the frequency of the electromagnetic wave. For dry, unperturbed snow, the scattering from the air/snow surface can be disregarded[Snehmani et al., 2010]. The volume of the dry snow is consistent of mostly air and snow particles, so the contribution from the volume of the snow pack can be seen as a function of the size of the particles [Snehmani et al., 2010]. The scattering from the three interfaces, air/snow surface scattering, volume scattering and snow/ground scattering is illustrated in Figure 4.1. For the snow in avalanche debris fields it is not entirely understood what causes the increase in backscatter. If it is extra volume scattering or increased surface scattering as a result of a rougher surface. For dry snow the volume scattering and ground backscattering can be written as follows:

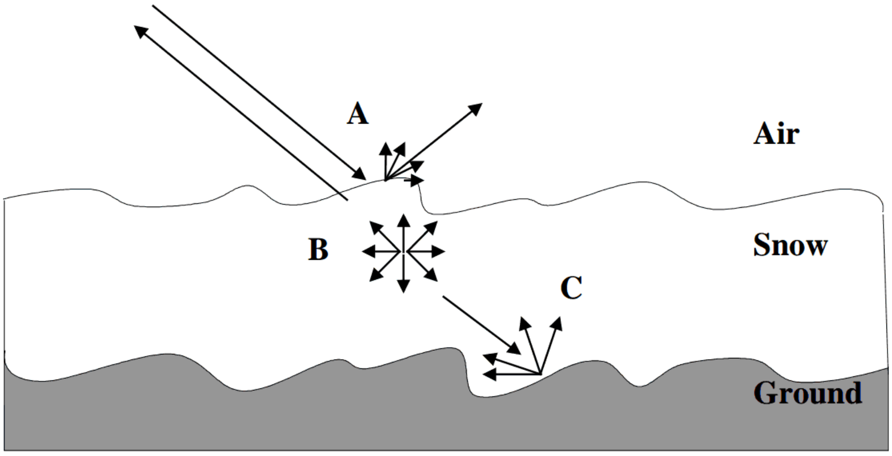

Figure 4.1: An illustration showing the scattering in the air/snow interface, volume scattering and scattering from the snow/ground interface. Illustration:[Koskinen et al., 2000]

$$\sigma_t = \sigma_v + \sigma_g \tag{4.1}$$

The volume scattering, σ_v is considered to be only from Rayleigh scattering and is described as:

$$\sigma_v = \frac{24\pi^4 r^3 v cos[\theta']}{\lambda^4 \kappa_e} |K|^2 [1 - L^{-2}[\theta']] \tag{4.2}$$

where r equals the snow crystal radius and v snow crystal volume. λ is the wavelength.

Surface scattering from the ground snow layer is a complex model, dependent on many variables. It can be approximated by the Michigan empirical surface scattering model described in [Oh et al., 1992].

In this thesis a reference image taken during the summer from the same radar location as the image where avalanches are included. When this image is subtracted from the original image, the difference should be the scattering that take place in the snow volume or on the surface of the snow pack in avalanche debris fields.

4.2 Radar backscatter in forest canopy

In [Imhoff, 1995] the effects of forest canopy on backscatter is investigated. The amount of vegetation surface per volume is found to be related with the backscatter coefficient σ, as well as the incident angle. In Figure 4.3 the reduction in backscatter can be seen as a function of incident angles and density of the forest. Also as the vegetation surface area increases the backscatter decrease.

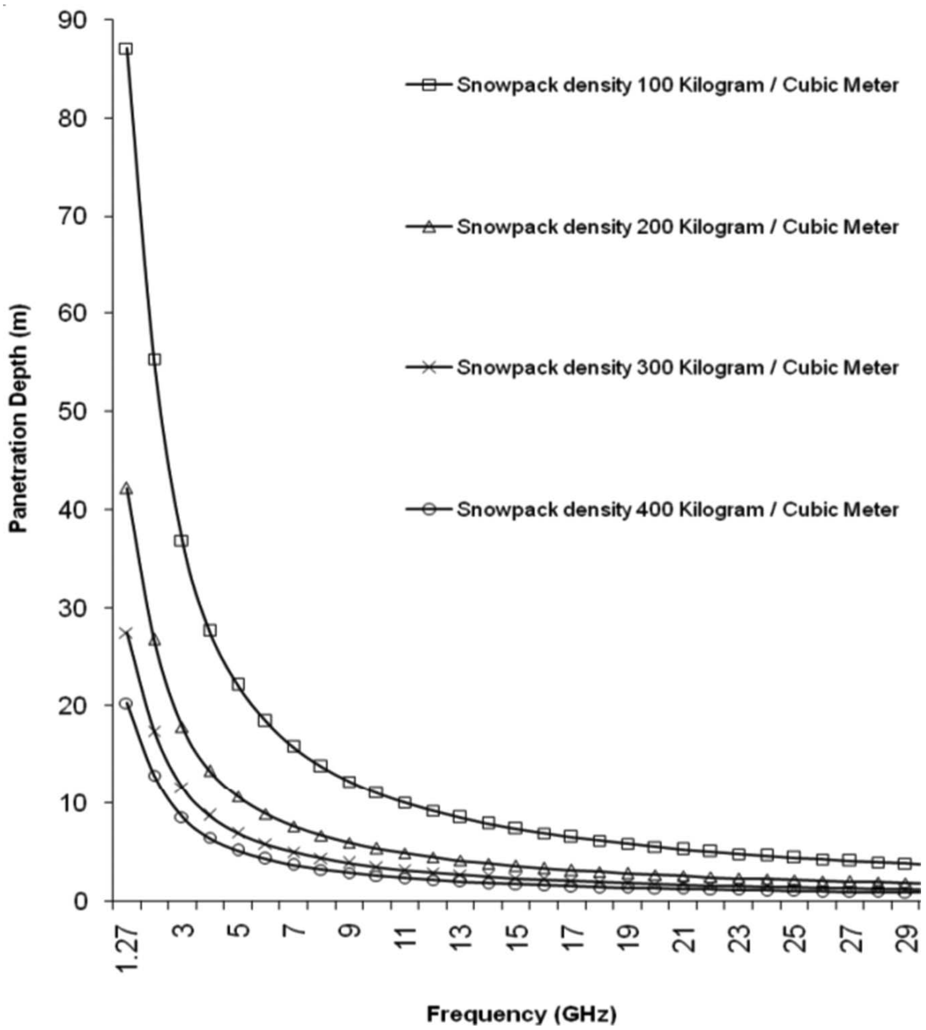

Figure 4.2: Change in penetration depth for different frequencies and densities of snow [Snehmani et al., 2010].

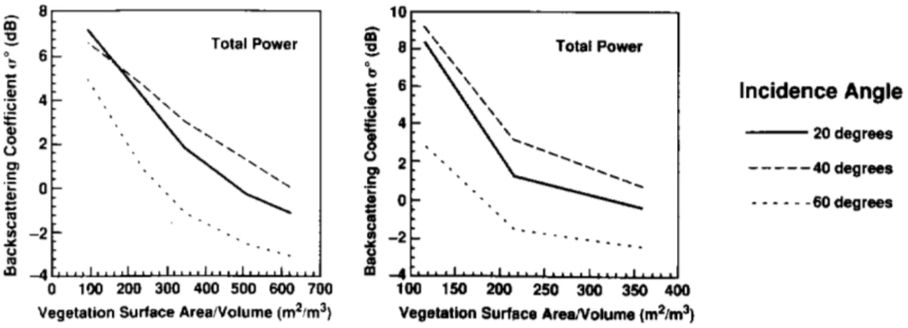

Figure 4.3: Effect of forest density and incident angle on backscatter coefficient σ. Left graph for 5kg/m^3 and right graph 15kg/m^3. Image from [Imhoff, 1995]

[Pivot, 2012] found an increase in backscatter from areas containing tree trunks during winter compared with areas with low vegetation (below 30cm in height). This combined with with [Imhoff, 1995] indicates a decrease in backscatter from forested areas from the winter to the summer is expected.

4.3 Liquid water content

Water has a large effect on microwave radiation and as the amount of liquid water in the snow increase, so does its absorption of the electromagnetic radiation. This cause an increase of the permittivity of the snow and an increase in volume scattering. The dielectric constant for wet snow can be calculated by a mixture model of Polder and Van Santen, [Magagi and Bernier, 2003].

$$\epsilon_m = \epsilon_d + \frac{W}{3} \sum_{j=a}^{c} \frac{\epsilon_w - \epsilon_d}{1 + \left[\frac{\epsilon_w}{\epsilon^+} - 1\right] A_j} \tag{4.3}$$

Where ϵ_m is the total dielectric constant for the snow layer, including water, air and ice. ϵ_d is the dielectric constant for dry snow, ϵ_w for water. A_j is the depolarization factor and W the volume fraction of the water. ϵ^+ is the effective dielectric constant of the enviroment which can be assumed to be equal to ϵ_d for small values of wet snow. For very wet snow, $\epsilon^+ = \epsilon_m$ [Magagi and Bernier, 2003]. In Figure 4.4 it is shown how the dielectric constant for electromagnetic radiation of different frequency change with an increase of water level in the snow. When the water level increase we see a higher dielectric constant at the air snow boundary and higher absorption in the snow layer, which in turn reduces the penetration of the snow layer [Pivot, 2012]. A decrease in backscatter is also observed in [Guneriussen et al., 1999] where the backscatter were measured from a snow covered area from April to June and a correlation between snow wetness and backscatter was observed.

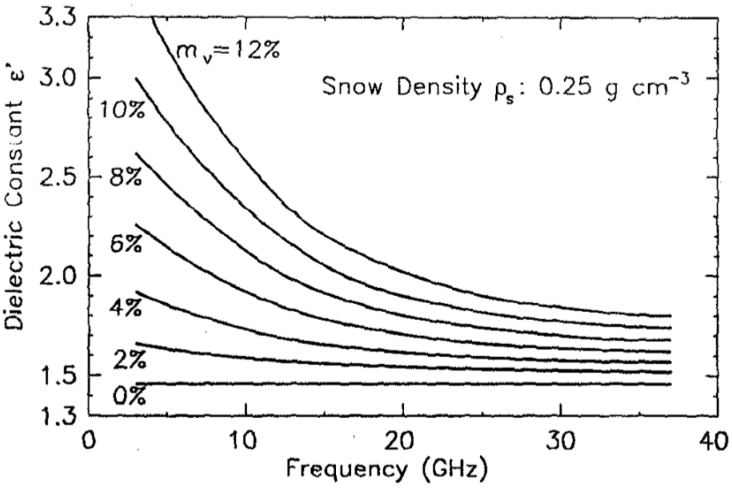

Figure 4.4: Increase of the dielectric constant at snow density ρ=0.25g/cm^3, and m_v=12% the water content in the ice. Image: [Magagi and Bernier, 2003]

Chapter 5

Method

In this chapter the methods created in this thesis will be presented together with the data available in this thesis. The data available are four images from RADARSAT-2, two winter images containing avalanches, and two reference images from the summer when the snow had melted. A Digital Elevation Model from Statens Kartverk is also available. The algorithms created in this thesis are explained in detail. All programming is performed in Matlab 2013b.

5.1 Datasets from RADARSAT-2 and Statens Kartverk

Three sets of data were available for this thesis. One set data set containing the reported avalanches in Tromdalen and on Kvaløya, another data set containing reference images that were ordered from the same areas during the fall of 2013 and a DEM delivered by Statens Kartverk.

Images with reported avalanches

The data were ordered by Norut after two large avalanches were reported in Troms, Norway. One on Kvaløya and the second on Senja, both can be seen in Figure 5.1. The images were taken by RADARSAT-2 in ultra-fine mode several days after the incidents, and were then geocoded with the GSAR software at Norut. This software also created masks so that areas containing geometric aberrations can be masked out. This software also multilooked the images to remove speckle, and this reduced the image resolution from 1.5m to 3m. On Senja the image was taken on the 5th of April 2013 at 16:35, and on Kvaløya the 9th of April 2013 at 16:19.

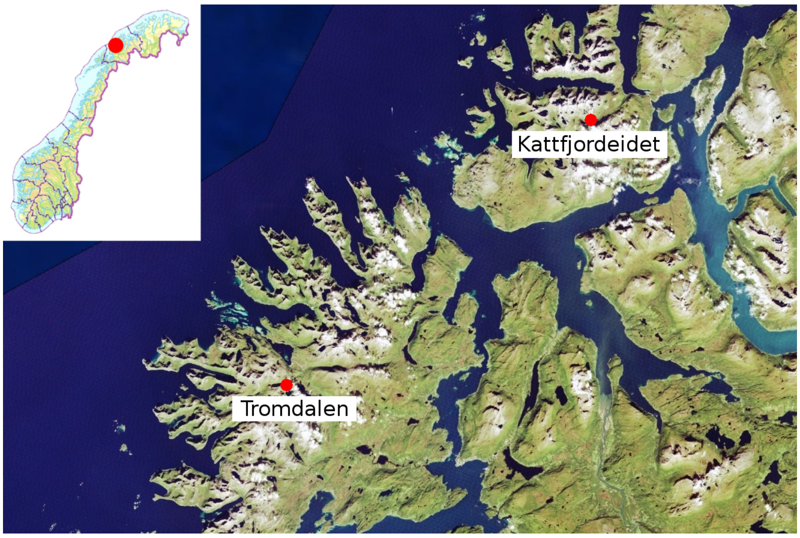

Figure 5.1: Map showing the locations of the two massive avalanches in Tromdalen, Senja, and Kattfjordeidet, Kvaløya.

Reference images

On a later date, 27th of August at 16:35 for Senja and 31st of August at 16:19 for Kvaløya, a second set of images were ordered for each site. This set was taken when the satellite was in the same location as the original images were, and these images are to function as a reference image. The backscatter from the reference image, should be equal to the backscatter from the images of the avalanches as the electromagnetic radiation is expected to penetrate dry snow as seen in Figure 4.2. In denser snow it is expected to see a higher volume or surface scattering, and since an avalanche compress the snow, a stronger backscatter signal is expected from sites containing avalanche debris fields or debris. Data of how the density in the snow change after an avalanche can be seen in table 2.1.

5.2 Digital Elevation Model

A DEM was delivered by Statens Kartverk, with a resolution of 10m which was resampled down to 3m to match the SAR images. This model was used to create a slope mask that masks away areas too steep, or too flat, to contain avalanche debris fields, and to make 3-D images of the sites containing avalanches to better visualize the surrounding slopes.

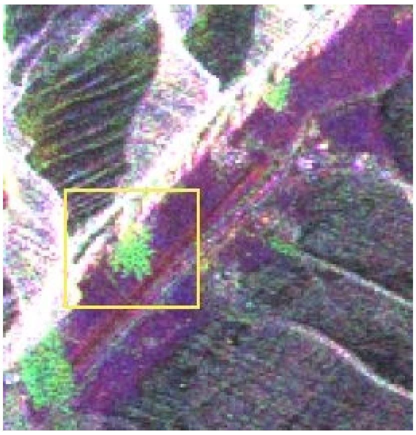

Figure 5.2: Image containing avalanche debris fields used in the green channel, causing avalanche debris fields to show as green. Image: [Wiesmann et al., 2001]

5.3 RGB images and locating subsets

An RGB image is made up of three 2D matrices, where each matrix is an intensity image. Each matrix makes up one of the colours in the RGB image. When the intensity for each pixel is the same for all the channels in the RGB image an averaged colour will appear, but if the intensity of one pixel in one of the channels is higher than the other two, this colour will be highlighted compared to the other two colours. This result can be observed in [Wiesmann et al., 2001] where the increase in backscatter from the avalanche debris fields highlights as green in the RGB image. This method require a reference image from the same area to be able to highlight the increased backscatter from the avalanche debris fields.

In Figure 5.2 from [Wiesmann et al., 2001] it can be notivced that the increased backscatter from the avalanche debris fieldin the green channel, match the cones from the avalanche in the aerial image very well.

After the RGB images were made, 10 subsets were selected, where 2 of the subsets are of the large avalanches that were reported on Senja and Kvaløya. The other 8 subsets include high backscatter areas that bear resemblance to avalanche debris fields, both in shape and location, and are therefore considered to be avalanche debris fields. For each of the subsets a manual drawn mask was created to be used when testing the accuracy of the filtering algorithm below. An example can be seen in Figure 5.5 and 5.6. Figure 5.3 shows a quick description of how the RGB images and the subsets are made, where data in has a orange background and data out, that will be used in later analysis, has a green background.

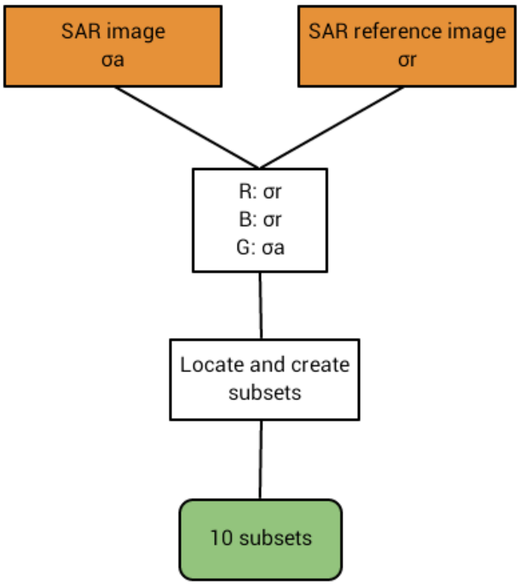

Figure 5.3: Both SAR images are used to create the RGB images, from where the subsets are selected.

5.4 Structure of the filtering algorithm

One of the goals of this thesis is to look at filters than can be fully used to make detection of avalanche debris fields easier and pave way for an automated system in the future. An algorithm was created to find the best filter, moving window size and threshold and consists of the following steps:

1. Using the subset coordinates from the RGB image to create subsets from σ_a and σ_r that will be used in the algorithm. Figure 6.1 and Figure 6.2.

2. Filtering each of the subsets with average, median, Lee sigma and Frost filters with different moving window sizes.

3. Using a threshold that vary from -1 to 3 to classify pixels as avalanche or not avalanche to create avalanche masks.

4. Calculating the accuracy the avalanche mask by comparing them with the manually drawn mask for each subset to check how many pixels are correctly classified as avalanche or not avalanche.

5. Return the best filter, moving window size and threshold for each of the subsets.

The algorithm is quickly be described in Figure 5.4, where the orange boxes are data in, and green box is data out

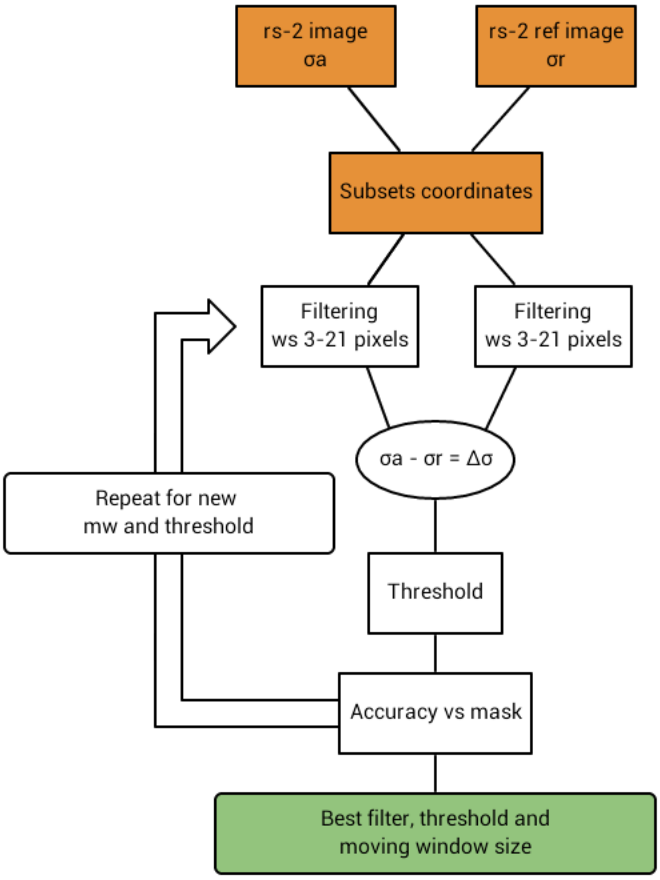

Figure 5.4: Both SAR images and subset coordinates are loaded into the algorithm before it finds the best moving window size, threshold and filter.

Subsets

After detecting possible avalanche sites in the RGB image the same coordinates were used to create subsets of σ_a and σ_r. These new subsets are used in the filtering algorithm.

Filtering

The filtering algorithm use four well known and well tested filters. The mean, median Lee Sigma and Frost filter are all used on the subsets created of σ_a and σ_r. The filters use a moving window where the calculations for a central pixel is performed. A for loop is used to vary the moving windows sizes from 3x3 pixels to 21x21 pixels before the $\Delta\sigma$ subset image is created by subtracting $\sigma_r - \sigma_a = \Delta\sigma$.

Thresholding

A threshold is created to separate the pixels into classes. In this case, a threshold is set to classify pixels as inside an avalanche or outside an avalanche.

After both the images containing the avalanches and the reference image have been filtered the reference image is subtracted from the the image containing avalanches as described above. Since C-band mircowaves have been shown to penetrate dry snow, see Figure 4.2, the scattering from the snowcovered areas should be more or less equal to the reference image for the same pixel neighbourhood an $\Delta\sigma$ image like Figure 3.8 is expected. Except in areas where snow have been perpetrated, as in avalanche debris. The threshold is calculated with the following pseudo code:

$$\begin{aligned} ifP_i &\leq T \\ P_i &= 1 \\ else& \\ P_i &= 0 \end{aligned} \tag{5.1}$$

$$\begin{aligned} &\text{where} \\ P_i &= \text{Pixel to be classified} \\ T &= \text{Threshold} \end{aligned}$$

When a pixel in the image has a value that is below the threshold, this pixel is classified as not avalanche. When the pixel has a higher value than the threshold the pixel is+ classified as avalanche. The minimum and maximum threshold for each image is chosen by testing a very large range of thresholds and observing the maximum and minimum threshold. It was found that the highest accuracy would lie between -1 and 3 for all the subsets.

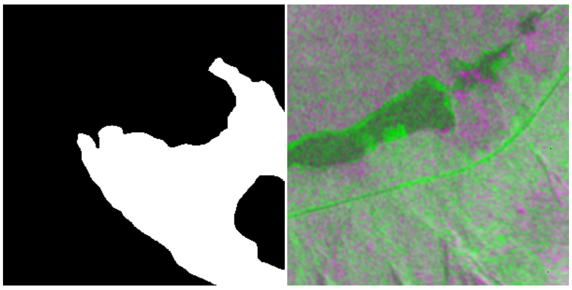

Figure 5.5: A manually created mask for a site 4 om Kvaløya is seen to the left. The right image is the subset for site 4, and a weak outline of higher backscatter can be seen

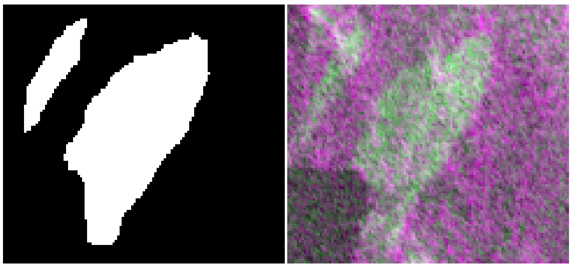

Figure 5.6: A manually created mask for site 1 on Senja is seen to the left. The right image is the subset the mask was created from and the high backscatter can be seen clearly against the surrounding areas.

Testing the accuracy

For each of the subsets a manually drawn mask was created. This mask covers the entire avalanche and other possible high backscatter areas, as the frozen lakes in as the goal is to see only the avalanche debris fields. For site 4 on Kattfjordiedet, see Figure 5.5 and Figure 5.6 for site 1 on Senja. The filtered and thresholded subset is compared to the mask for each iteration for the size of the moving window and threshold. The final result is stored for later use. The accuracy of the filtering algorithm is measured in how many pixels are classified correctly compared with the manually drawn mask.

Returning the best variables

When the filtering algorithm is finished, the best filter, moving window size and threshold for each subset is returned for later use.

5.5 Creating a slope mask from a Digital Elevation Model

By calculating the gradient for each pixel in the Digital Elevation Model (DEM), the slope is found for every pixel. When the gradient is calculated, the function used finds the largest gradient between the central pixel and the nearest neighbouring pixels. The variance is then calculated for each pixel and this new variance matrix will be used to create the slope mask.

Each of the subsets coordinates are used to create new subsets from the variance matrix. Finding the maximum and minimum values for each of the subsets gives a measure of what interval of variance avalanche debris fields can be expected to be found in. Values that are outside of the interval are areas where there is low likelihood for avalanche debris fields to be found and subsequently masked out. This allows for a slope mask to be created. Figure 5.7 describes how the slope mask is created, where data in is marked in orange, and data out is marked in green.

5.6 Applying all results to a final image

After finding the best filters, moving window sizes and threshold with the filtering algorithm, the average of all the sites, 1 to 10, is calculated for all the variables. These values are used to filter the complete images of σ_a and σ_r and to create an avalanche mask. The avalanche mask is multiplied with the slope mask to remove all areas that are too steep or too flat for avalanche debris fields to be located there. This final avalanche mask now shows all areas with a relative high backscatter in slopes where avalanche debris fields are likely to be found. Geometric aberrations are masked out with the masks provided by Norut, before all masks are laid on top of the RGB image created earlier and all areas with pixels classified as avalanche is marked in red. The process of reaching the final product is described in Figure 5.8 and data in is marked with orange and data out in green. The in data is created in the earlier algorithms.

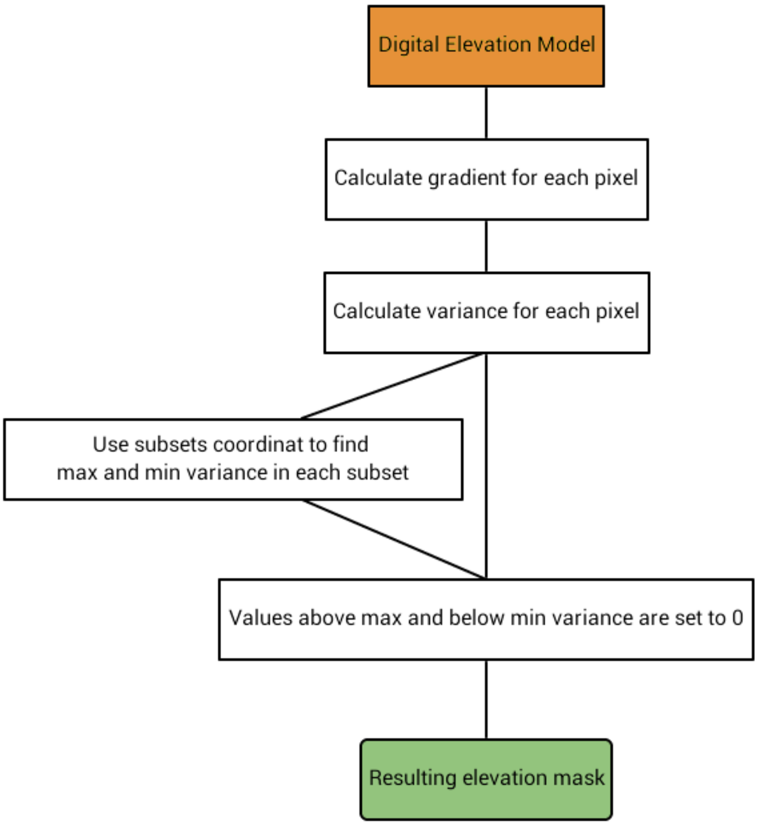

Figure 5.7: The gradient is derived from the DEM provided, then the variance is calculated before the maximum values of the local variance inside each subset is found and a slope mask is created.

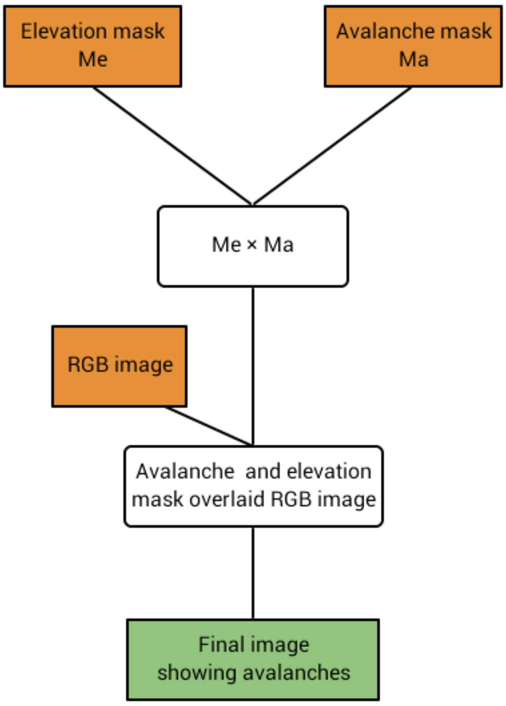

Figure 5.8: The final process of creating a product that show all areas where it is likely that avalanche debris fields are found.

Chapter 6

Results and discussion

Here the results from the algorithms are studied and discussed. Starting with the filtering algorithm that finds the best threshold, moving window size and filter for the subsets that were visually located in the RGB image. Following is the calculation and creating of the slope mask and the final part where the masks are applied to the RGB image and avalanche debris fields are marked.

6.1 RGB images and subsets

In [Wiesmann et al., 2001] RGB images were created using 3 images taken at different times. The image containing the avalanche was used as the green channel and two other reference images used as red and blue channels. This caused the increase in backscatter from the avalanche to show up as green avalanche debris fields. This was also done on the images from Kvaløya and Senja and two RGB composition were created. The image containing the avalanche debris field was used in the green channel whereas the reference image as blue and red. On a large subset we can clearly see the stronger backscatter from the avalanche debris fields in the image from Kvaløya and Senja. One large area from the Kvaløya and two large areas from Senja were selected when it was observed several avalanche debris field in these large areas. These areas can for future reference be seen in Figure 6.1, 6.2, and 6.3. In each one these figures avalanche debris field can be seen inside the marked squares.

6.2 Filtering Algorithm

The major avalanche and three other sites that are likely to include avalanche debris fields were chosen from the RGB image from Kvaløya, the sites are marked 1-4 on Figure 6.1. From the image of Senja, 6 sites are found, where 3 are located in the vicinity of the large avalanche reported avalanche in Tromdalen. They can be seen in Figure 6.3 and are marked 4 to 6. Also three other realtive strong

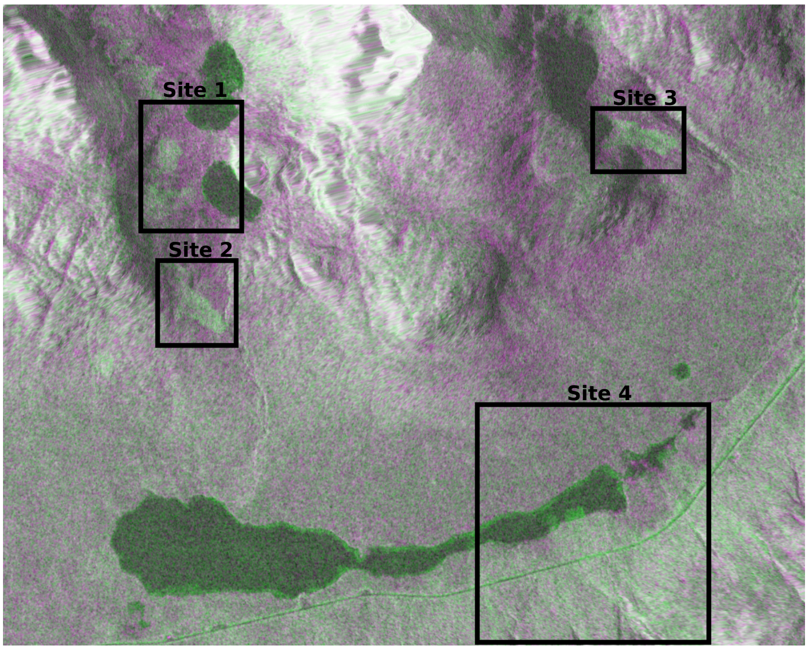

Figure 6.1: A large subset over Kattfjordvannet on Kvaløya. 4 subsets containing avalanche debris fields are marked, where the large reported avalanche is found in Site 4.

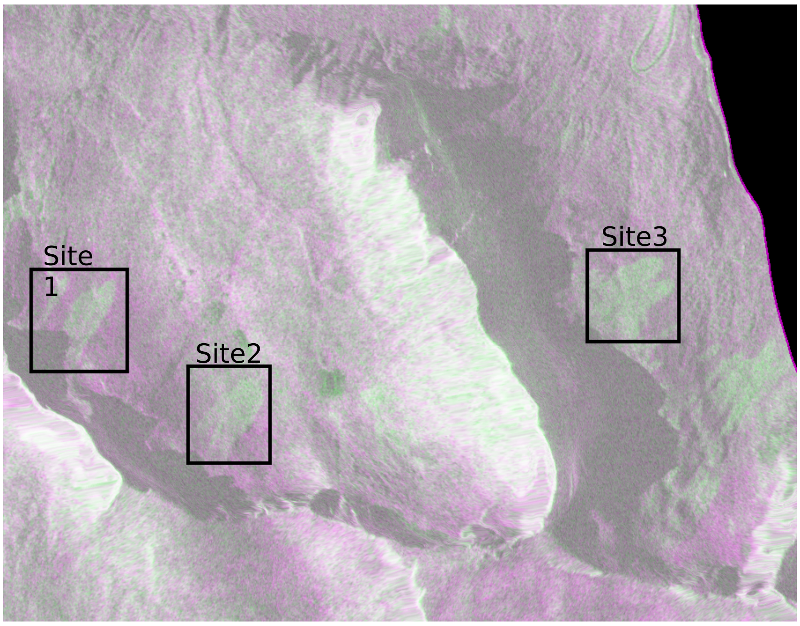

Figure 6.2: A large subset on Senja that contains several small avalanches. These subsets are marked as Site 1 to 3

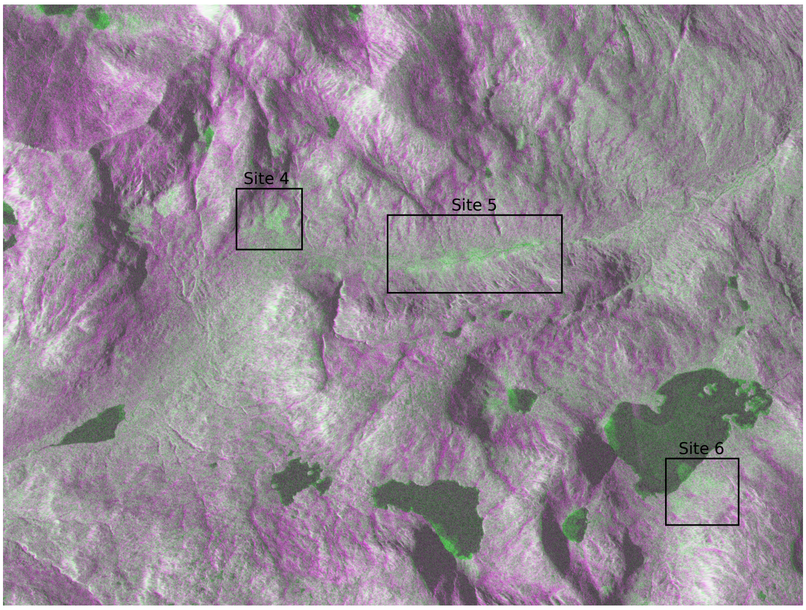

Figure 6.3: The second large subset on Senja. Here the fatal avalanche is found in Site 5, and two smaller avalanche debris fields are seen in site 4 and 5

backscatter areas were located in a area to the east on the Senja image. They can be seen in Figure 6.2 and are marked site 1 to 3.

The algorithm described in Section 5.4 was used on all sites to calculate the size of the moving-window, filter and the threshold that performed best for each of the individual sites. The algorithm finds the best filter and plots the percentage of correctly classified pixels, compared with the manually drawn mask. With the thresholds used along the x-axis and the accuracy along the y-axis. The size of the moving windows can be seen in the annotation.

The plots for each site contains the best performance for each filter, where threshold and moving window size can be seen. Accurate numbers for each of the sites can be found in 6.1.

Site 1 Kvaløya

This site was chosen because of its diffuse form neighbouring the waters edge. A main avalanche debris field can be observed in the middle of the image, and another smaller avalanche towards the bottom of the image. From the graph in Figure 6.4a it can be observed that the median filter, with the largest moving windows size, is the filter that has the highest accuracy. But the other 3 filters also have a high accuracy in classifying the pixels correctly. The best filter for site 1 on Kvaløya is the Median filter, together with a moving window of size 21x21 pixels with a threshold of 1.3. It also has a accuracy, where 87,55% of the pixels in the subset correctly. In Figure 6.5a the avalanche mask created by the filtering algorithm can be seen and compared with the manually drawn

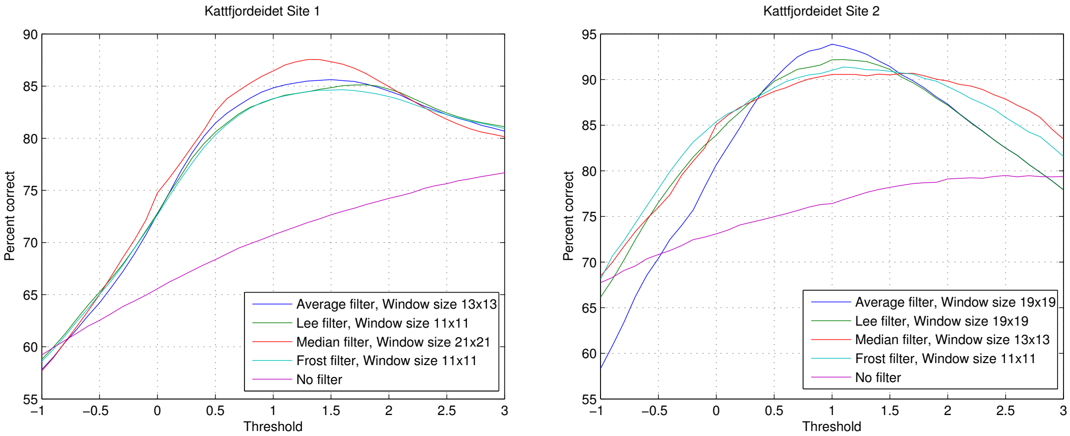

(a) (b)

Figure 6.4: The best performance of each of the filters, calculated by the filtering algorithm. Site 1 on Kvaløya (a) and Site 2 on Kvaløya (b).

mask in Figure 6.5b.

Site 2 Kvaløya

Site 2 on Kvaløya was chosen as a site because of its distinction against the area surrounding it. It is very easy to locate as the contrast between the avalanche debris field and the surrounding area are very clear on the RGB image in Figure 6.1. This allows for a very accurate mask to be drawn and a high percentage of correctly classified pixels is expected. In Figure 6.4b the best moving window size and threshold are plotted. For site 2 the average filter has the highest accuracy with a moving window size of 19x19 pixels and a threshold of 1. The amount of pixels that are correctly classified is at 93,88% which is what was expected since the avalanche is easily visually distinguishable from its surrounding. In Figure 6.6 the mask created by the filtering algorithm (a) can be compared with the manually drawn mask (b).

Site 3 Kvaløya

Site 3 on Kvaløya was chosen for the same reason as site 2. The avalanche can be seen in Figure 6.1 and is very distinguishable from its surroundings and a high accuracy is expected. The orientation is almost the same as in site 2, therefore it is also expected that both moving window size and threshold should be somewhat similar. From the graph in Figure 6.7a one can observe that for this site the average filter is the best. The window size is large, 21x21 pixels and the threshold is 1, the same as for Site 2. The amount of correctly classified pixels are also very high at 98,88%. This is as expected from the two similar sites of 2 and 3. In Figure 6.8a the avalanche masked created by the algorithm can be observed and compared with the manually drawn mask in Figure 6.8b.


(a) (b)

Figure 6.5: (a) The avalanche mask created by the best performing filter for Site 1 on Kvaløya by the filtering algorithm, the white areas are classified as avalanche. (b)The manually drawn mask.

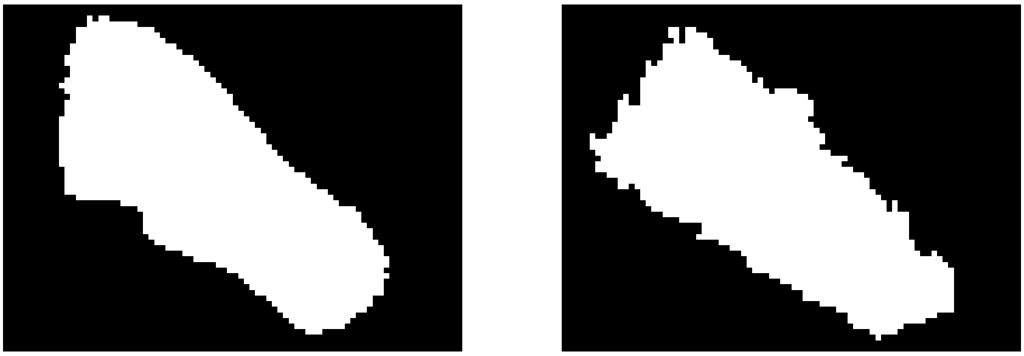
(a) (b)

Figure 6.6: (a) The avalanche mask created by the best performing filter for Site 2 on Kvaløya by the filtering algorithm, the white areas are classified as avalanche. (b)The manually drawn mask.

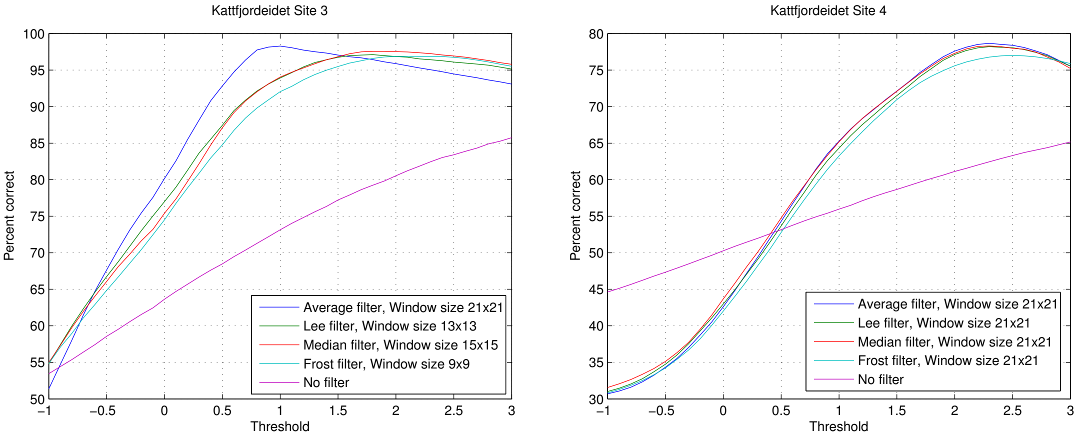

(a) (b)

Figure 6.7: The best performance of each of the filters, calculated by the filtering algorithm. Site 1 on Kvaløya (a) and Site 2 on Kvaløya (b).

(a) (b)

Figure 6.8: (a) The avalanche mask created by the best performing filter for Site 3 on Kvaløya by the filtering algorithm, the white areas are classified as avalanche. (b)The manually drawn mask.

(a) (b)

Figure 6.9: (a) The avalanche mask created by the best performing filter for Site 4 on Kvaløya by the filtering algorithm, the white areas are classified as avalanche. (b)The manually drawn mask.

Site 4 Kvaløya

The last site on Kvaløya includes the avalanche that is has the best verification of the two reported avalanches on Kattfjordeidet and Tromdalen. This avalanche, seen in Figure 6.1, is very hard to distinguish from its surroundings. It is therefore not expected that the filtering algorithm will return a high accuracy for this site compared to the 3 other sites. From the graphs in Figure 6.7b it can be seen that all the filters perform almost identically. But also here the average filter comes out on top, though marginally, with a moving window size of 21x21, threshold of 2.5 and accuracy of 76,95%. This is surprisingly well classified considering how hard it is to distinguish the avalanche from its surroundings, compared to the other 3 sites. The mask created by the filtering algorithm can be seen in Figure 6.9a and the manually drawn mask in Figure 6.9b

The same procedure was followed for the 6 sites on Senja. The 3 first sites are from a large subset to the east, Figure 6.2, whereas the 3 last are from the area around the large and fatal avalanche in Tromdalen, Figure 6.3.

Site 1 Senja

Site 1 can be observed in Figure 6.2 of Senja. The site was chosen because it is very distinguishable from the surroundings and site 2 and 3 have the same orientation, form and size. Because of that it is expected that all three sites should result in moving window sizes, thresholds and accuracy to be more or less equal. From the graphs in Figure 6.10a it can be observed that all the filters are performing almost equally well, but the median filter is slightly better than

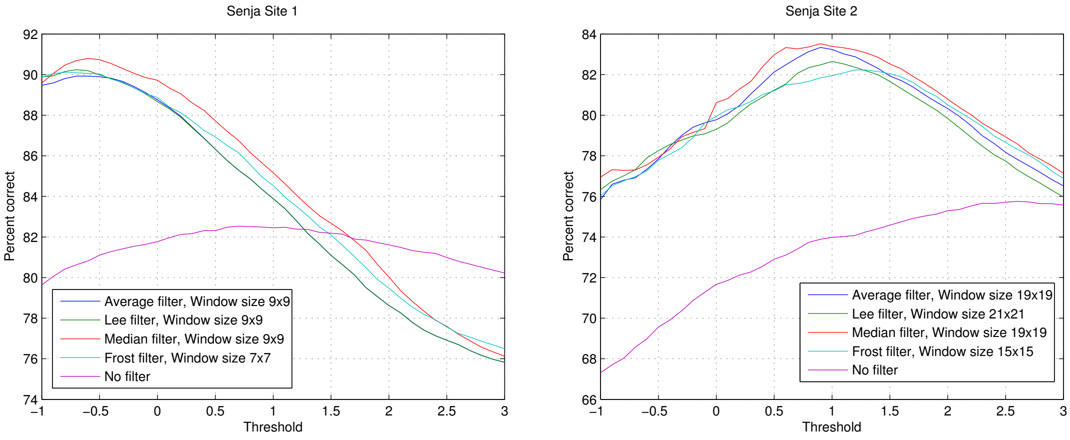

(a) (b)

Figure 6.10: The best performance of each of the filters, calculated by the filtering algorithm. Site 1 on Senja (a) and Site 2 on Senja (b).

the other. This is achieved with a window size of 9x9 pixel, threshold of -0,5 and 90,2% of the pixels very correctly classified. This best accuracy for each of the filters can be seen in Figure 6.10a

In Figure 6.11a the filtered image can be seen and compared with the manually created mask in Figure 6.11b.

Site 2 Senja

The second site, Figure 6.2, is strikingly familiar with the two other sites when looking at the shape, orientation and size so its expected to see a similar result for the threshold, moving window and filter as Site 1 and 3.

The median filter is the best performing filter with a moving window size of 19x19 pixel, threshold of 0,9 and only 83,52% correctly classified pixels. This result is unexpected since the avalanche have the similar orientation, shape and size as the avalanche in Site 1. In Figure 6.10b the best performance for each of the filters can be seen, and in Figure 6.12a the avalanche mask created by the filtering algorithm can be compared to the manually drawn mask in Figure 6.12b.

Site 3 Senja

For the 3rd site, Figure 6.2, the Lee filter has most pixels classified correctly. It correctly classifies 96,06% of the pixels with a moving window size of 11x11 pixels and a threshold of -0,1. This site was also expected to be similar to site 1 and 2 due to reason already mentioned. In Figure 6.13a the best accuracy of each filter can be observed, and in Figure 6.14a the best mask created by the best filter can be compared with the manually drawn mask in Figure 6.14b.

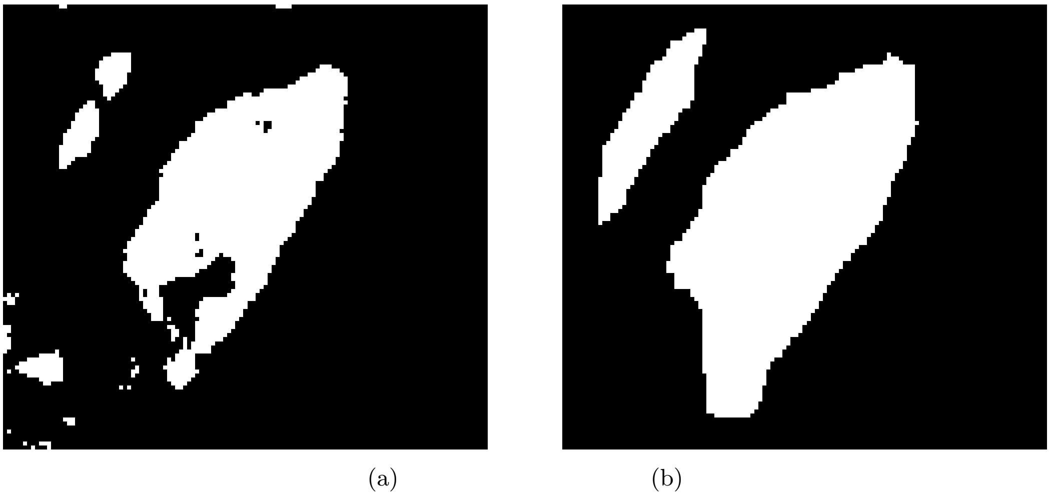

(a) (b)

Figure 6.11: (a) The avalanche mask created by the best performing filter for Site 1 on Senja by the filtering algorithm, the white areas are classified as avalanche. (b) The manually drawn mask.

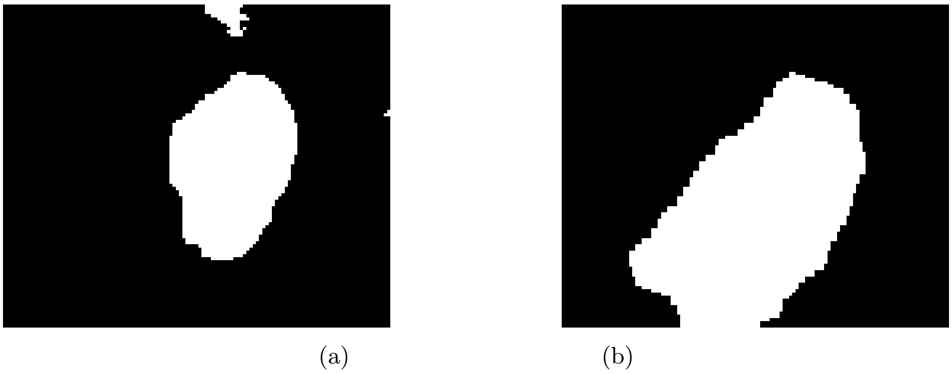

(a) (b)

Figure 6.12: (a) The avalanche mask created by the best performing filter for Site 2 on Senja by the filtering algorithm, the white areas are classified as avalanche. (b) The manually drawn mask.

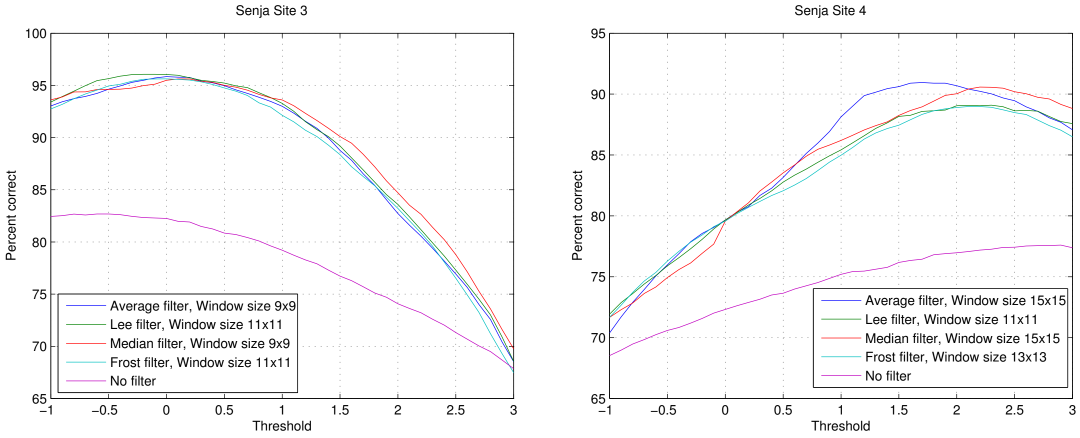

(a) (b)

Figure 6.13: The best performance of each of the filters, calculated by the filtering algorithm. Site 3 on Senja (a) and Site 4 on Senja (b).

(a) (b)

Figure 6.14: (a) The avalanche mask created by the best performing filter for Site 3 on Senja by the filtering algorithm, the white areas are classified as avalanche. (b) The manually drawn mask.

(a) (b)

Figure 6.15: (a) The avalanche mask created by the best performing filter for Site 4 on Senja by the filtering algorithm, the white areas are classified as avalanche. (b) The manually drawn mask.

In Figure 6.14a and 6.14b the avalanche mask created by the filtering algorithm can compared with the manually drawn mask.

Site 4 Senja

This site has an avalanche that is very easily distinguishable on the top/northern side whereas the bottom of the avalanche seems to dip into an area where there is a generally higher backscatter, see Figure 6.3. The complexity of this avalanche makes it an interesting case when testing the filtering algorithm. The result was that the average filter, with a moving window size of 15x15 pixels and a threshold of 1,5 managed to classify 90,2% of the pixels correct. This was also somewhat surprising as a lower accuracy was expected due to the more diffuse bottom part of the avalanche. In Figure 6.13b the best accuracy of each filter can be observed, and in Figure 6.15a the best mask created by the best filter can be compared with the manually drawn mask in Figure 6.15b.

Site 5 Senja

Site 5 is where the fatal avalanche on Senja happened. It stopped in a narrow valley with steep slopes on both sides. From the RGB image, Figure 6.3, it is not easy to spot the classical avalanche shape as seen in most of the other sites. The areas with a relative higher backscattering is located in the bottom of the valley

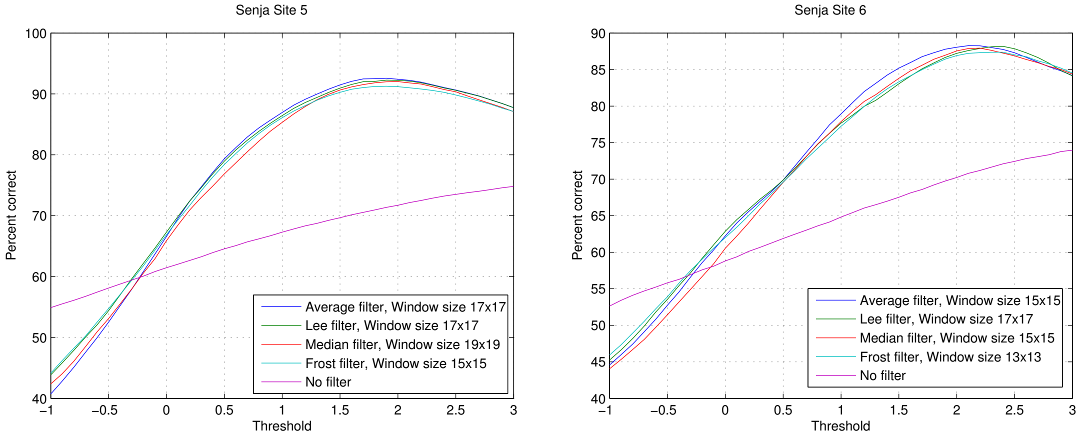

(a) (b)

Figure 6.16: The best performance of each of the filters, calculated by the filtering algorithm. Site 5 on Senja (a) and Site 6 on Senja (b).

(a) (b)

Figure 6.17: (a) The avalanche mask created by the best performing filter for Site 5 on Senja by the filtering algorithm, the white areas are classified as avalanche. (b) The manually drawn mask.

in several larger debris fields that are somewhat connected. This corresponds well with the report from NGI that was written after the incident [Brattlien, 2013]. The best performing filter was the average filter which classified 96,06% of the pixels correctly. This was achieved with a moving window of size 17x17 pixel and a threshold of 1,9. In Figure 6.16a the best accuracy of each filter can be observed, and in Figure 6.17a the best mask created by the best filter can be compared with the manually drawn mask in Figure 6.17b.

The filtered and thresholded image ended up very closely to the mask as can be seen in Figure 6.17a and 6.17b.

Site 6 Senja

The last site, Site 6 on Figure 6.3, was chosen to test the filtering algorithm on an avalanche that has a part of its debris field on a frozen lake. The avalanche is also quite easy to distinguish from both the slope its originating from and the lake. Here the average filter classified 88,27% of the pixels correctly with a moving window of size 15x15 pixels and a threshold of 2,1. In Figure 6.16b the best accuracy of each filter can be observed, and in Figure 6.18a the best mask

(a) (b) 6.1

Figure 6.18: (a) The avalanche mask created by the best performing filter for Site 6 on Senja by the filtering algorithm, the white areas are classified as avalanche. (b) The manually drawn mask.

created by the best filter can be compared with the manually drawn mask in Figure 6.18b.

The avalanche mask created by the filtering algorithm can be studied in Figure 6.18a and compared with the manually drawn mask in Figure 6.18b.

6.2.1 Summary of the filtering algorithm for the subsets on Kvaløya and Senja

On Kvaløya the avalanche masks created by the filtering algorithm had a good accuracy with an average 89.15%. In table 6.3 the filters, moving window sizes and the thresholds that had the highest accuracy for each site can be seen. When comparing the figures of the avalanche mask created by the filtering algorithm and the manually drawn mask it can be observed that for Figure 6.5a and 6.5b, from site 1 on Kvaløya, that the smaller debris field to the left, are shrunk quite a bit in the mask created by the filtering algorithm. The reason for this shrinking could be the median filter smoothing the edges of the avalanches and especially if the contrast between the avalanche and the surroundings are low. The two lakes in the right of the masks have maintained their shapes quite well, and a new area of pixels classified as debris field can be observed in the far left of the image. This area could very well be a part of the original debris field, but it was not included in the manually drawn mask.

In site 2, Figure 6.6a and 6.6b the filtered avalanche mask has a strong resemblance the manually drawn mask. This is also the case for site 3 in Figure 6.8a and 6.8b. Both these avalanche debris fields have a very strong contrast between the avalanche and the surrounding areas, this gives reason to believe that these sites should be have a high accuracy as there are few areas that can be mixed up with the surrounding areas.

For the large avalanche in site 4, a shape corresponding to the manually drawn mask, Figure 6.9a, can be seen in the filtered avalanche mask, Figure 6.9b. The part of the avalanche that runs out onto the frozen lake, the area from the lower right corner up towards the lake and the second smaller runout to the right of the avalanche are all observable.+ The road that runs through the site can be seen continuing out of the avalanche next to the lake. The shape of the mask is identifiable it is clear that much of the avalanche and the surroundings are disrupted by erroneously classified pixels. The avalanche in site 4 passed through a forest and broke most of the threes in its path. These broken tree stems could have added to the volume scattering in the avalanche debris fields to increase the contrast, but in this case this did not happen. Instead is the entire avalanche is very hard to distinguish from its surroundings as the surroundings also have a relatively strong backscatter. This could be explained with the dense forest growing in that area as is discussed in Section 4.3.

All the exact moving window sizes, threshold and filters that had the highest accuracy for each site can be seen in Figure 6.1

Site	Filter	Size	Threshold	Percent correctly classified
Site 1	Median	21x21	1,3	87.55
Site 2	Average	19x19	1	93.88
Site 3	Average	21x21	1	98.28
Site 4	Average	21x21	2,3	78.51

Table 6.1: The best filter and the variables that allowed for the highest accuracy of classified pixels for the sites on Kvaløya.

The first three sites on Senja, 1-2 and 3 were expected to yield similar results due to the similarity of shape and orientation. But the results from these three sites were very different from each other. Site 1 had the lowest threshold of all the sites at -0.5 when using a surprisingly small moving window of size of 9x9 pixels. While site 3 has a threshold of -0.1 with a moving window size of 11x11. This is the only site where the Lee filter is the best performing filter and it has a very high accuracy of 96.06%. Site 2 is more like the other sites with a threshold of 0.9 and window size of 19x19. The reason for the negative threshold could be caused by wet snow surrounding the avalanche, and the stronger backscatter signal is created by the roughness of the surface of the avalanche. This is described in Section 3.8 and can be studied in Figure 3.9 and is a possible solution to the low backscatter from these sites.

In site 1 in Figure 6.11a the smaller avalanche to the left is reduced from a singular debris field to two smaller fields. Also there are some debris behind the main avalanche. The reason for the shrinkage of the smaller left avalanche can be the median filter smoothing the edges of the avalanche and therefore more of the pixels falls below the thresholding and are classified as not avalanche. In Figure 6.11b the manually created mask can be seen with a whole smaller avalanche to the left and no debris behind it. This debris in Figure 6.11a could very well be debris or large chunks of snow left behind by the avalanche.

Site 4 on Senja surprised with a high accuracy rate during the classification, and this was unexpected because of the relative high backscatter surrounding the avalanche around the lower boundaries. In Figure 6.17a the filtered avalanche mask can be seen to be very similar to the mask.

In site 5 (Tromdalen) the avalanche is not easy to locate or identify without prior knowledge of its location. It is located in the bottom of a narrow and steep valley and bear no resemblance with the other avalanches in shape. The deposits are wedged in the bottom of the valley and have not had the natural runout that can be observed for the other avalanches. This site does however, have a very strong backscatter compared to the slopes surrounding it. In Figure 6.17a the avalanche mask created by the filtering algorithm can be seen to bear close resemblance to the manually drawn mask in ref. 6.17b.

Site 6 includes two avalanches, where one of them runs out onto the frozen lake. The manually created mask in Figure 6.18b have close resemblance with the avalanche mask created by the algorithm. Both avalanches can be seen in Figure 6.18a, and the runout of the larger avalanche can be seen on the frozen lake. The debris field on the lake can be seen on in fig 6.18a and the filtering algorithm classified the lake and the debris field on the lake with high accuracy.

The algorithm does a fairly good job, not only in classifying pixels, but also in removing larger clusters of relatively high backscatter from the areas surrounding the avalanche. An exception is around the large avalanche in site 4 on Kvaløya. Several large areas with erroneously classified pixel are observed, the frozen lake, the road and in the forest covering the area the avalanche passed through. The lakes have a higher backscatter in the winter than during the summer, this leads to a difference when $\Delta\sigma$ is made and they will therefore be classified as avalanches. The forest can cause a greater backscatter from the stems of the threes as described in

The average of the threshold, moving window and filter for each of the large subsets were calculated and can be found in Table avg to be used on the larger subset before testing a total average on the full images from Kvaløya and Senja

Site	Filter	Size	Threshold	Percent correctly classified
Site 1	Median	9x9	-0,5	90,2
Site 2	Median	19x19	0,9	83,52
Site 3	Lee	11x11	-0,1	96,06
Site 4	Average	15x15	1,5	90,95
Site 5	Average	17x17	1,9	92,58
Site 6	Average	15x15	2,1	88,27

Table 6.2: The best filters and the variables that allowed for the highest accuracy of classified pixels for the sites on Senja.

Area	Window size	Threshold	Best filter	Accuracy
Area 1, Kvaløya	21x21	1.45	Average	89.15
Area 2, Senja	13x13	0.1	Median	89.92
Area 3, Senja	15x15	1.83	Average	90.6

Table 6.3: The average threshold, moving window size, filter and accuracy for each area.

6.3 Applying average values from the filtering algorithm the a larger area

Values from table 6.3 were used to filter larger subsets of Kvaløya and Senja to create an avalanche mask that was added to the RGB image.

The result for Area 1, Kvaløya, can be seen in Figure 6.19. Here it can be observed that by using the average values from table 6.3, it still is easy to identify the avalanches in site 2 and 3. Site 1 has clearly to few pixels classified as avalanche compared to the RGB image, whereas the large avalanche in site 4 is very hard to distinguish. Several large areas of obviously misclassified pixels can be seen in and around Site 4, the road and the frozen lake and the birch forest all have relative high backscatter. The lakes surrounding Site 1 are also classified as avalanche debris fields.

Over the first large are Senja, see Figure 6.20, the three sites from earlier are easily detectable. Site 3 is the site where most of the avalanche is covered by the avalanche mask, and at site 2 some green high backscatter areas can be seen between in slope above the avalanche. In site 1 the right avalanche is covered by the mask, but the smaller one to the left has large parts of it not covered by the mask. It was expected that site 3 would have the best result as the mean threshold used when filtering the larger image, lie closer to the true threshold value for site 3, the threshold was -0.1, see Figure 6.2. Due to the averaging of the threshold, filter and moving window size it is possible that both avalanches are more in compliance with the manually drawn mask with other values for threshold and moving window size. The last large area over Senja, Area 2, see Figure 6.21, all three sites are well covered by the avalanche mask created by the filtering algorithm. And especially the large avalanche in site 5 is very well covered. Site 4 can be seen to be touching the high backscatter area below it, but the shape of the avalanche is well covered by the avalanche mask. Site 5 is well classified even over the frozen lake.

It is easy to recognize several large areas that are false positives in these two images. Especially frozen lakes, roads and forest give relative high backscatter and are therefore classified as avalanches. The forests give a higher volume scattering because of the stems of the trees as shown in section 4.2. While the frozen lakes has a much higher backscatter from the ice, than it has from the reference image when the ice is gone.

6.4 Creating and applying the slope mask

In order mask away as much as possible of areas where the possibility for avalanche debris fields are very small, a DEM model is used. After calculating the gradient and variance of the gradients for each pixel for the whole DEM, the coordinates from the subsets seen in figures 6.1, 6.2 and 6.3 are used to create subset from the DEM. For the DEM subsets the maximum value of the variance inside each subset is found, see table 6.4, and for the minimum, a value close to 0 is chosen. Values that are found to be higher than the maximum value from all the sites are said to be an area with low probability of avalanches and are

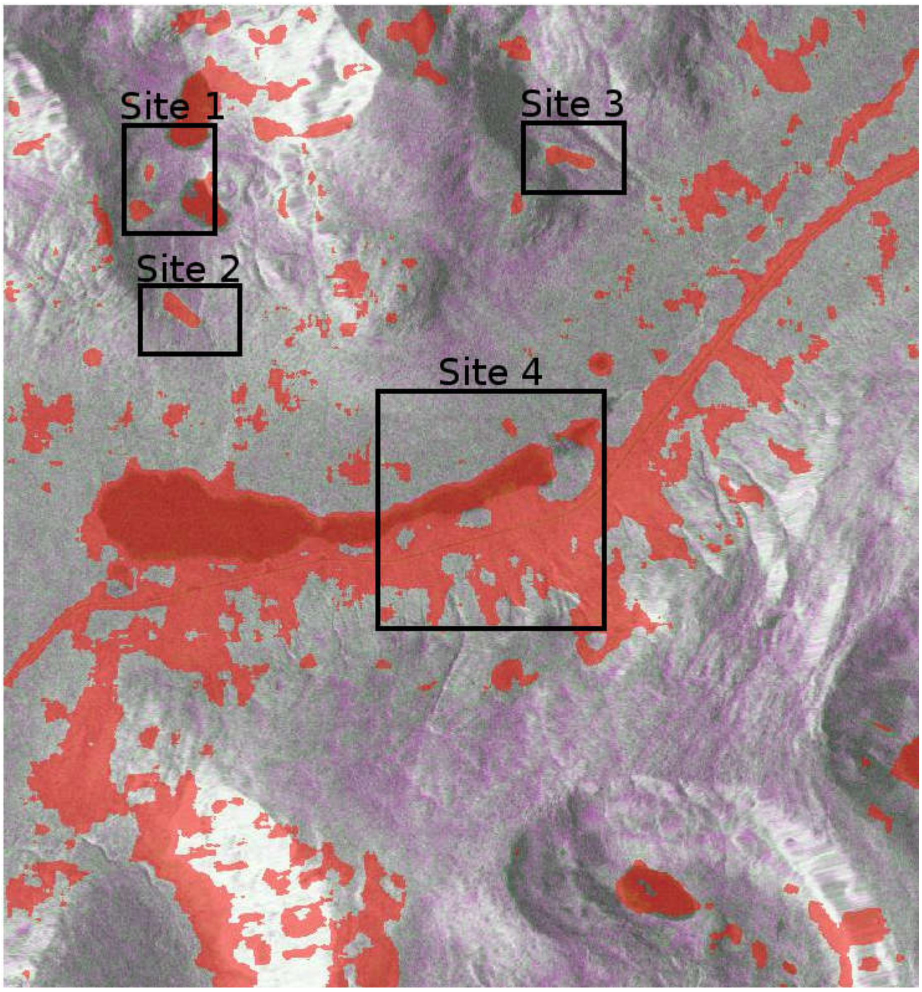

Figure 6.19: The avalanche map created by the filtering algorithm is added to a larger RGB image over Kvaløya. Note all the frozen lakes are labelled as avalanche debris fields.

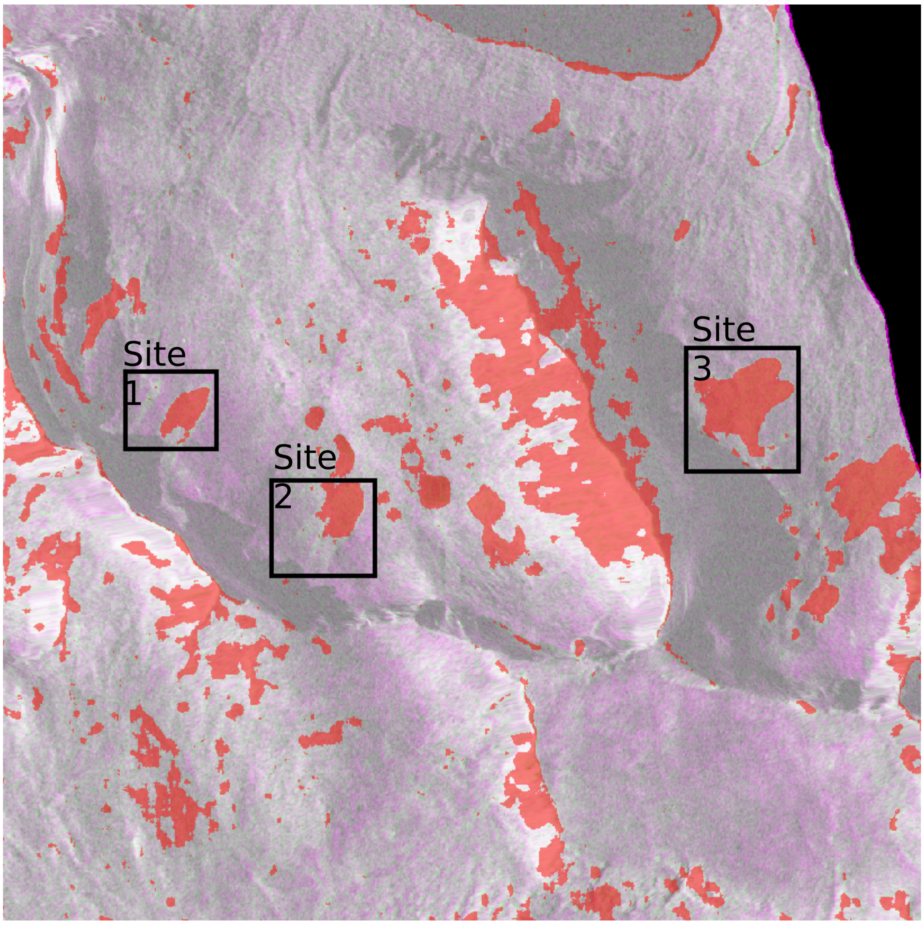

Figure 6.20: The avalanche map created by the filtering algorithm is added to a larger RGB image over Senja. Large areas that are classified as avalanche debris fields can, amongst other, be seen on the mountain ridge between site 2 and 3.

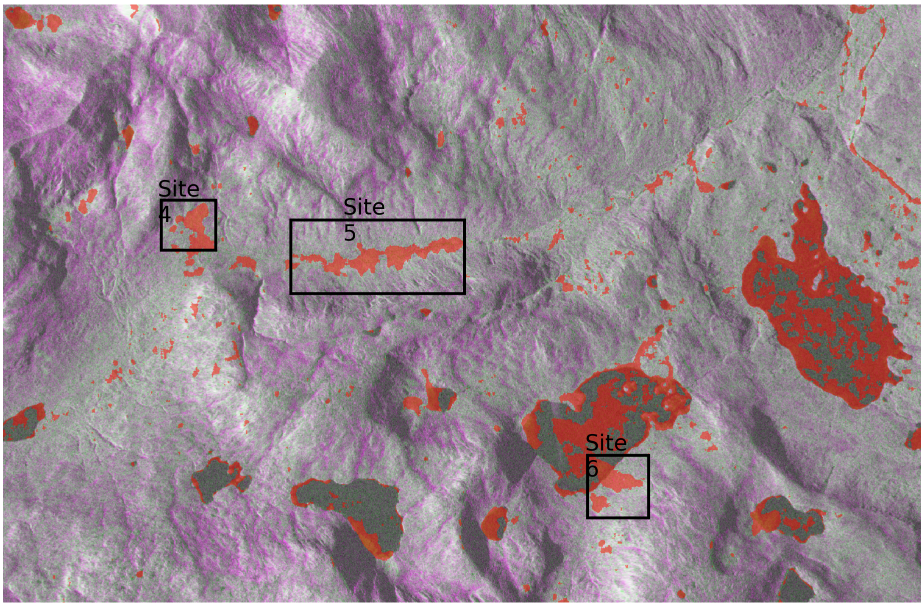

Figure 6.21: The avalanche map created by the filtering algorithm is added to a larger RGB image over Senja. Large areas of pixels classified as avalanche debris field are seen on the lakes and the shore lines.

masked out. Values that are found to be below the minimum value of all the sites are also said to have a low probability for avalanches, this include lakes and roads. By using a very low minimum value, areas that a close to flat will be included inside the range of possible avalanche debris fields, but not areas that are entirely flat. Like the area in site 4 on Kattfjordeidet where the avalanche has a runout on a very flat area and also the lake. The near flat area will be included while the runout on the lake is removed. This is an assessment that was made, as the frozen lakes and flat areas create more noise in the avalanche mask than the importance of including avalanche runout. In Figure 6.21 and 6.19 the frozen lakes show a relatively high backscatter and are therefore classified as avalanche by the filtering algorithm. This creates many erroneously classified areas in the avalanche mask, so by eliminating lakes from the elevation mask a better mask is created. This could possible be avoided, and the avalanche runouts on lakes included, if a water mask was available and shrunk by such an extent that possible avalanche runouts and deposits on the lake would not be excluded from the elevation mask.

The elevation mask is using values of 1 and 0, where 1 are areas with variance that can be found inside the variance range of the 10 sites, and 0 are areas with a variance outside that range. When observing Table 6.4 the difference in variance between Senja and Kvaløya is obvious. This means that the avalanches on Kattfjordeidet all have stopped in steeper slopes than the avalanches on Senja, and especially the avalanche debris field in Site 3 seem to have stopped in a steep area.

Adding the elevation mask to the Figure 6.1, 6.2 and 6.3 new images are created with avalanche and elevation masks included.

In Figure 6.22 it can be observed far less pixels classified as avalanches, when compared to Figure 6.19, and the lakes are now removed as possible debris fields, but also the furthest runout of the large avalanche in site 4 have been removed from the lake. There are still some areas left on the shorelines as well as on ridges and in the high mountains. These areas might be masked out when the geometric distortion masks from the GSAR software is added. The road have been removed to some extent but are still visible in the left of the image.

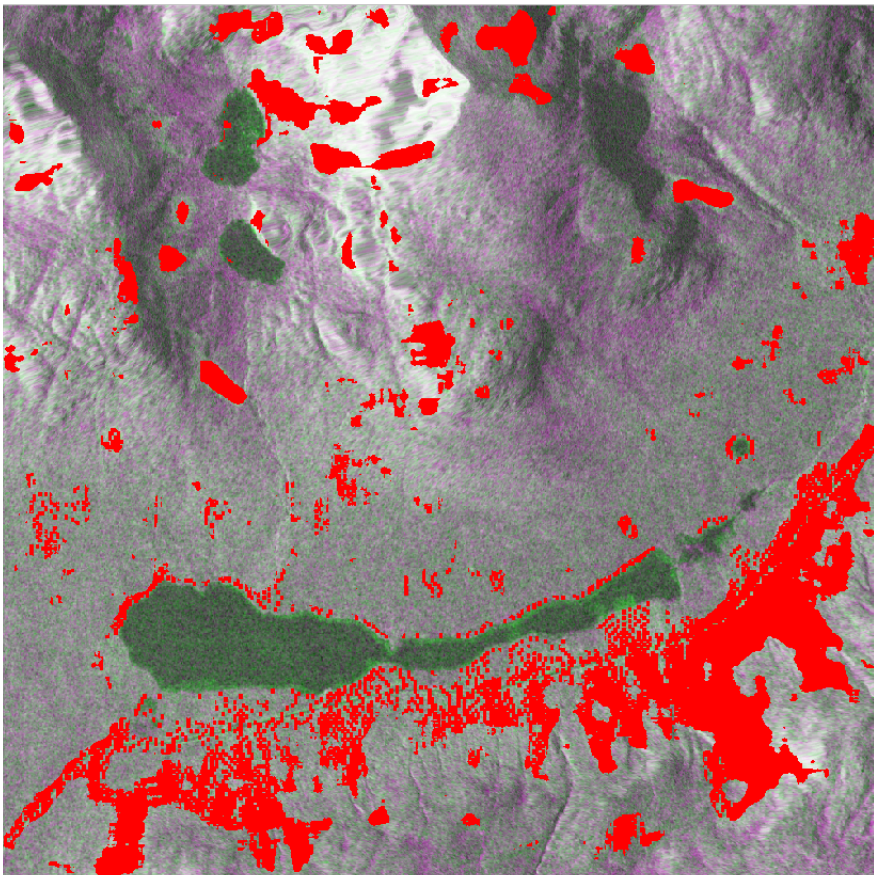

Figure 6.22: Image of Kattfjordeidet on Kvaløya, the avalanches in Site 2 and 3 can be seen very well, whereas the large avalanche, site 4, is lost in surrounding pixels classified as avalanches. Site one is still observable, but have lost some of its edges

For site 1 to 3 on Senja, the avalanches in site 1 and 3 are still easily detectable, and they correspond well with the area of high backscattering in the RGB image well. In site 1 it can also be observed that the smaller narrower avalanche to the left of the avalanche seen in Figure 6.23 have disappeared completely. This is most probably due to the average filter smoothing the edges until the narrow avalanche is completely filtered away. It is observed that some disintegration in the lower part of the avalanche in site 2 has occurred, this was introduced after the elevation mask, so its natural to assume that the elevation mask have masked out the lower ends of this avalanche as it has a runout zone on very flat land. A 4th avalanche can be seen to the right of the third avalanche. On the RGB image this avalanche has a strong backscatter, but it was not included when the sites were chosen. Here large clusters of possible avalanche debris fields can be seen behind the main deposit.

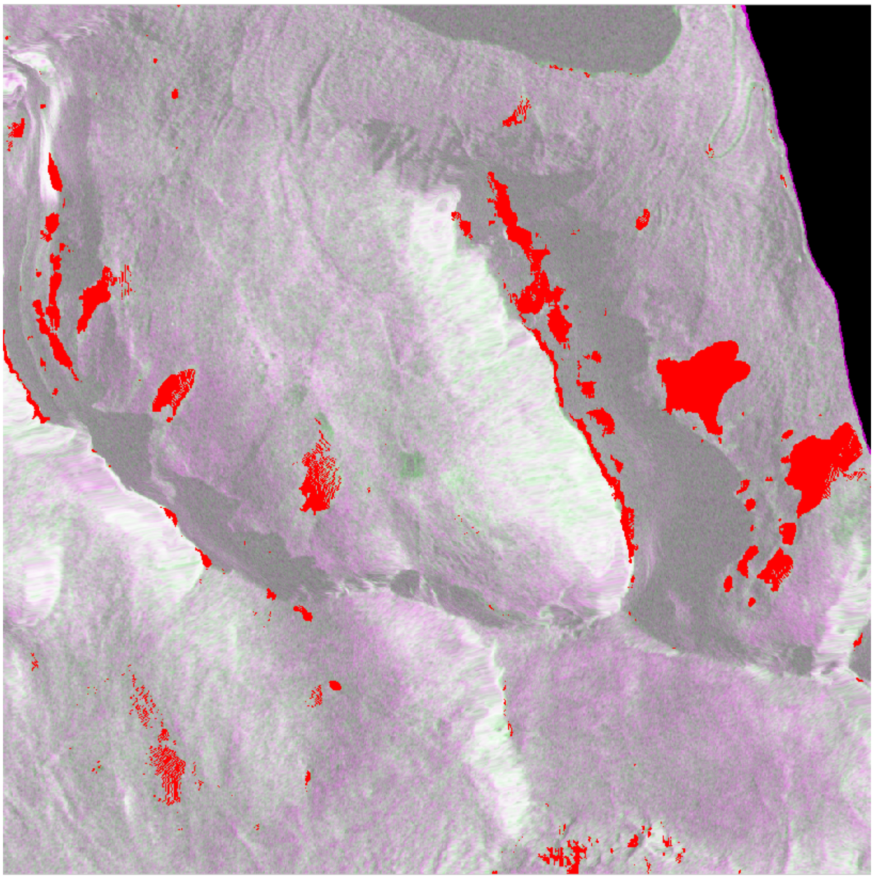

Figure 6.23: Image of Area 1 on Senja, the avalanches in Site 1, 2 and 3 can be seen very well.

In the last area on Senja, Figure 6.24, the first site has been classified correct along the upper boarder where there was a clear contrast in the RGB image, whereas the lower boarder is indeed touching another high backscatter area that also has been classified as avalanches. The large avalanche in Site 5 is very easily detectable as well but some disintegration have occurred amongst the middle of the deposit where it is natural to assume that the valley is quite flat. The two avalanches in site 6 are still very visible, but the lower runout of the avalanche to the right is now removed along with many strong scatterers in and around the lake. A road can still be observed to the far right of the image.

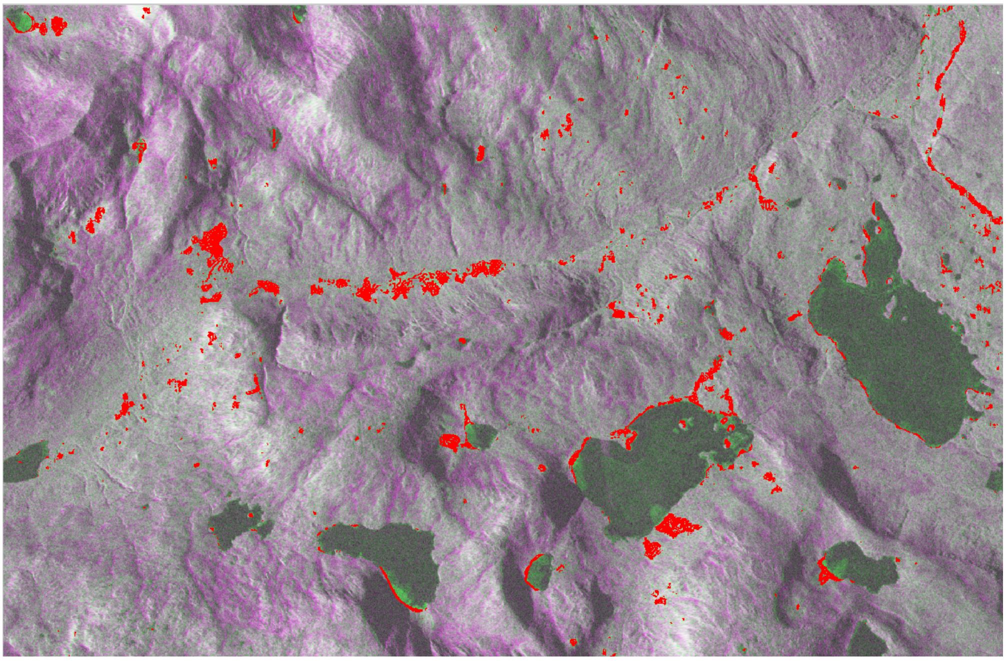

Figure 6.24: Image of Area 2 on Senja, the avalanches in Site 4, 5 and 3 can be seen very well, but the run out on the avalanche in site 6 is removed from the image.

Site	**Max variance**
Site 1, Kvaløya	12.25
Site 2, Kvaløya	2,25
Site 3, Kvaløya	33.40
Site 4, Kvaløya	9.18
Site 1, Senja	0,25
Site 2, Senja	0,56
Site 3, Senja	0,25
Site 4, Senja	0,25
Site 5, Senja	0,25
Site 6, Senja	0,27

Table 6.4: The maximum variance inside each of the sites on Senja and Kvaløya.

6.5 Fully automated avalanche detection

By following the method described in 5.6 and values from Table 6.5 the full SAR images from Senja and Kattfjordeidet was filtered and avalanche masks were created. The low threshold in site 1 and 3 on Senja, Figure 6.13a and 6.13a, was ignored. For site 1 the accuracy is still above 80% with a threshold of 1.5 and for site 2 the accuracy is above 90% with a threshold at 1.5 with the median filter. Therefore are the values from these two sites not included in the average threshold as they would have caused much reduction. The moving window size, threshold and filter is then calculated to be:

Site	**Max variance**
Filter	Average
Threshold	1,52
Moving window size	17x17

Table 6.5: The average threshold, moving window size and filter for Senja and Kvaløya.

By observing the other filter graphs in Figure 6.4, 6.7, 6.10, 6.13 and 6.16 it can be observed that all the filters, with exception of site 4 on Kvaløya, have an accuracy of above 80%, which is considered acceptable for this purpose, when using a threshold of 1.52.

By using the filter settings from table 6.5 on the full SAR images, avalanche masks were created. The elevation masks were created for the full DEMs, and the geometric aberrations masks created by the GSAR software were added to remove areas with shadowing, foreshortening and layover.

In Figure 6.25 the final product of the avalanche mask, elevation mask and the geometric aberrations mask can be seen for the full image of Kvaløya. All the lakes in this image are now excluded from the avalanche mask which is coloured in red. The avalanches in the original sites are all still visible. Several new areas are now now classified as avalanche. By creating 3D models of the new sites it is apparent that these new sites classified as avalanches can be avalanche debris fields.

In Figure 6.26 an avalanche debris field can be observed, below an area masked out by the geometric mask created by the GSAR software. It is possible that the avalanche have travelled through this area and stopped below as deposits can be seen in a narrow valley.

Figure 6.28 is from the south side of the image in Site 6. Here a large debris field can be seen in the middle of valley, and several other smaller deposits above the large one. These deposits can have originated from the steep areas on the peak above it. large area of geometric aberrations covers the side of the peak.

In Figure 6.27 three possible avalanches can be seen and deposits or debris are observable in the slope towards the valley floor.

For Senja, see Figure 6.29, there are far less pixels classified as avalanche, and especially in the regions near the top of the peaks. Both images are run through the same algorithm for avalanche detection, and several new possible avalanche debris fields are detected nearby, marked site 7 to 9.

In site 9, Figure 6.30, a very clear debris field can be observed below a steep slope. Another avalanche classified cluster can be seen above it. This is possibly a deposits left behind by the avalanche before it came to a stop at the main deposit.

In Figure 6.31 a debris field can be seen in the bottom of the valley, while another debris field is seen high above on a ledge in the slope. The avalanche

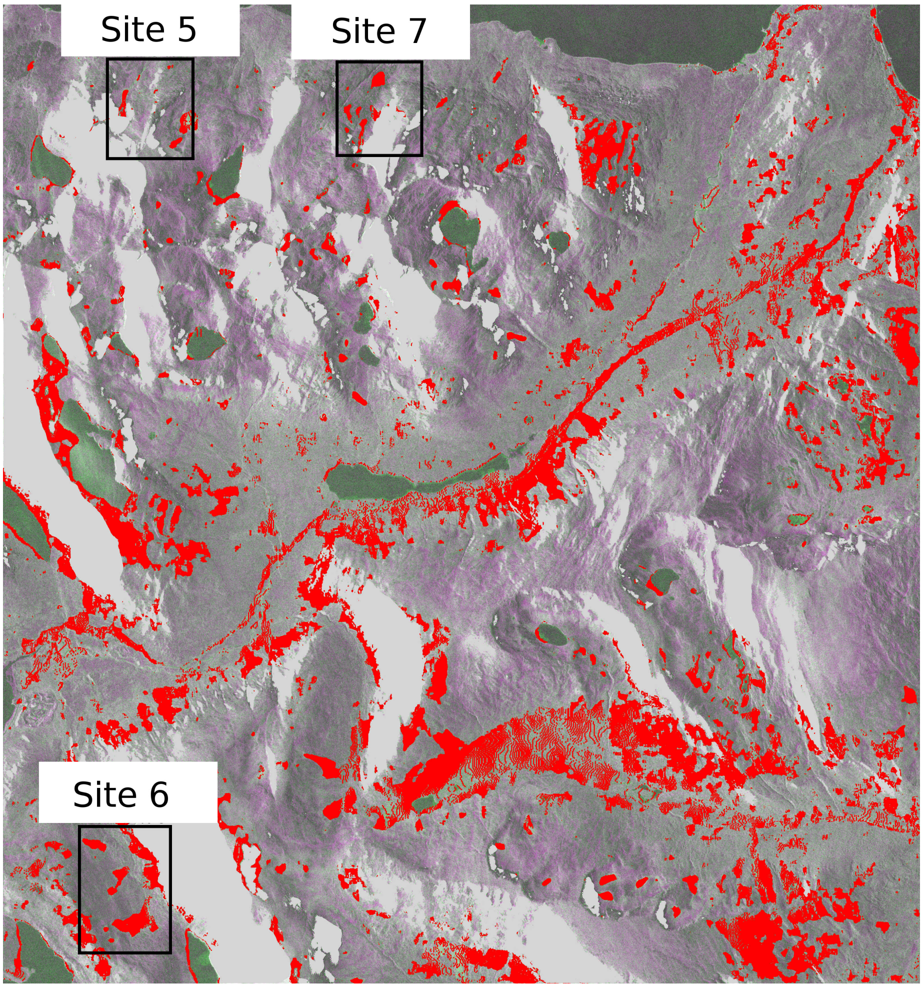

Figure 6.25: The avalanche mask slope mask and geometric aberrations mask is added to the image over Kvaløya. 3 new sites with avalanche debris field are marked

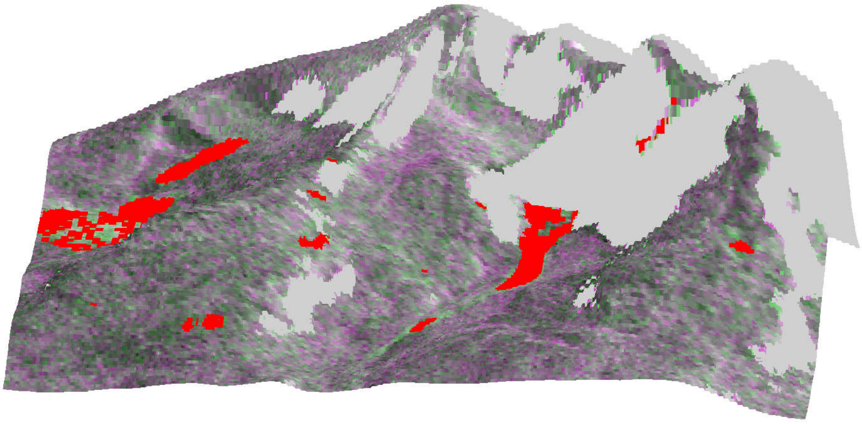

Figure 6.26: 3D image of Site 5 on Kvaløya, the area to the right are classified as avalanche and can be observed an area masked out by the geometric masks. This indicate a steep slope above the avalanche debris field.

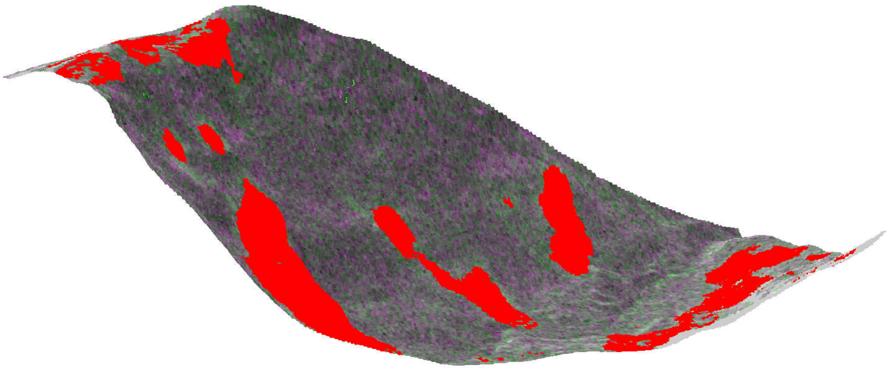

Figure 6.27: 3D image of Site 6 on Kvaløya, 3 large avlanche debris fields can be seen stretching down a steep slope towards a valley. Above the largest one, left, some smaller clusters can be seen as well some areas on the top.

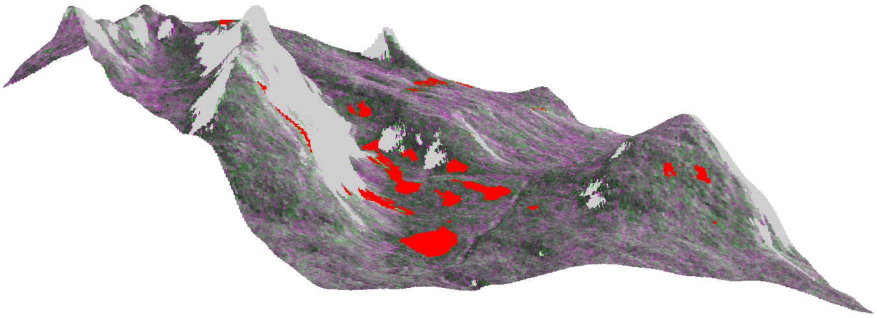

Figure 6.28: 3D image of Site 7 on Kvaløya, the areas classified as avalanche can be observed below steep slopes that are masked out with the geographic mask.

have possibly started on the upper parts of the mountain and left a debris field behind on the ledge, before accumulating more snow in the steep slope below.

In Figure 6.32 an avalanche debris field can be observed innermost in the valley. Another avalanche is possibly observed to the right in this figure, where it has debris fields in a narrow valley before stopping before or on the frozen lake. Also to the bottom left part a long avalanche debris field can be observed following a narrow valley before fanning out at the bottom.

The filtering of the full SAR images with the values from table 6.5 and adding the avalanche masks, slope masks and the geometric mask to the image shows a clear image where the areas classified as avalanche debris fields are coloured red. On Kattfjordeidet, Figure 6.25, there can be seen several areas where there are misclassification of the avalanche mask. These areas can be explained with a heavy rain in the days before the reference image was taken for Kvaløya, 2.4. This can have reduced the the general backscatter from the reference image and resulted in a higher backscatter in the $\Delta\sigma$ image for some areas. Also in the far right on Kvaløya a birch forest is located in the valley where a relative strong backscatter signal is seen. This can be explained by Section 4.2. The backscatter is reduced in a forest canopy and increased by the stems of trees in a winter forest, meaning a weaker backscatter signal will be observed during the summer.

On Senja far less such large areas with obvious misclassification can be found. In the days before the reference image was taken from Senja there was very little rain compared to Kvaløya. This could be the reason for the lack of such areas on Senja as the soil was less saturated and therefore had a stronger backscatter signal in the reference image

On both images there can be observed areas with higher backscatter that are not classified as avalanche debris fields, even if their location is prune to avalanches. A probable solution to this is that the debris fields seen in those location are of an older that. An older avalanche might have a weaker backscatter than a fresh one. This can be verified by either having verified and dated avalanches

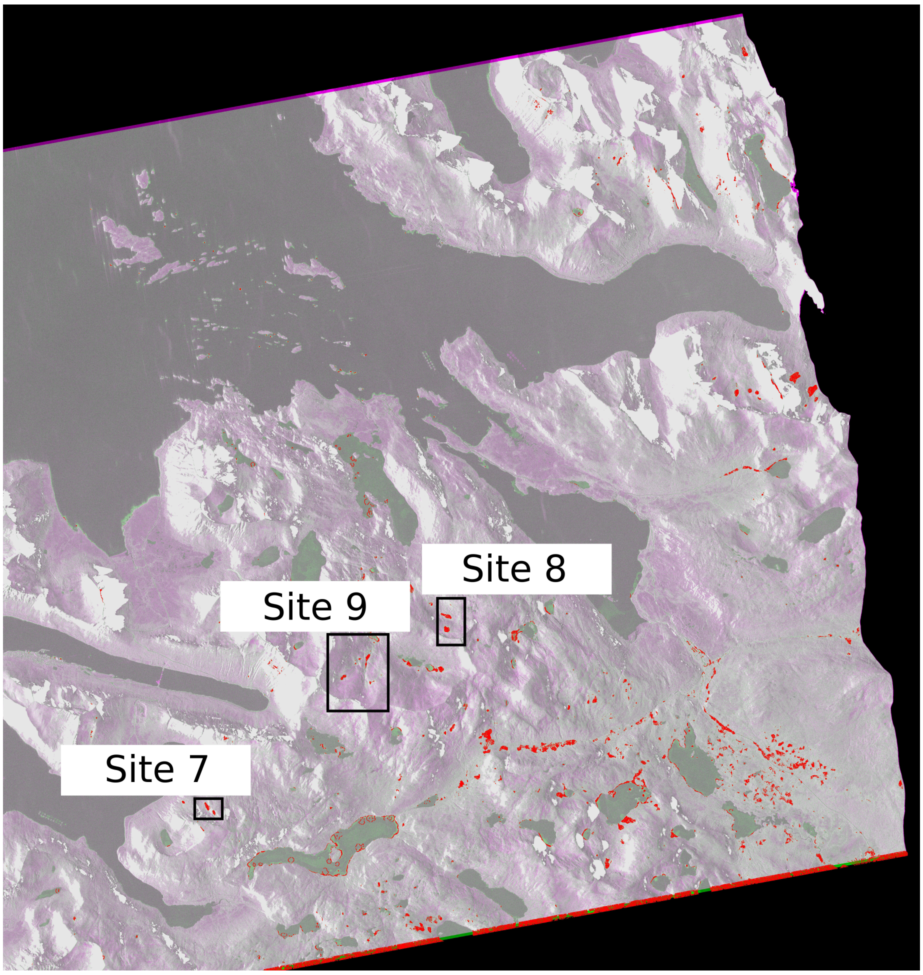

Figure 6.29: The avalanche mask, slope mask and the geometric aberration mask is added to the image over Senja. 3 new sites with avalanche debris field are marked

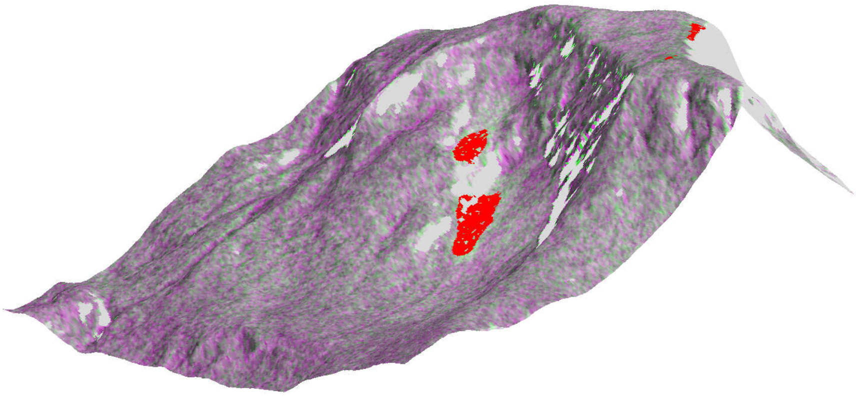

Figure 6.30: 3D image of Site 7 on Senja, A debris field can be seen in towards the bottom of a steep slope and a cluster of debris is left behind further up a possible avalanche path.

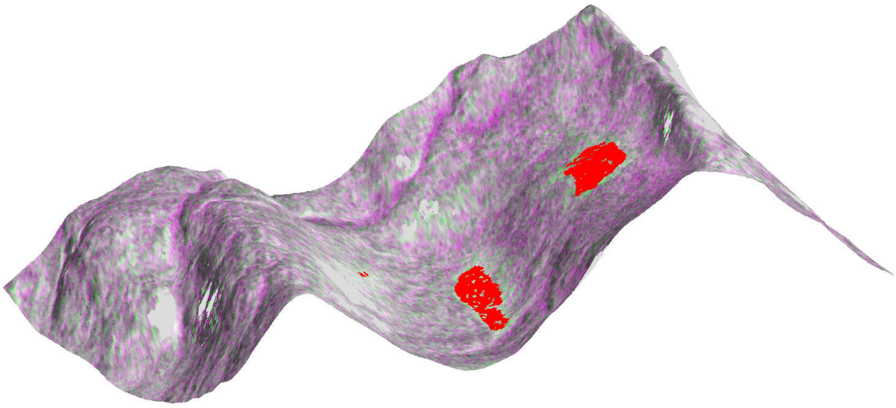

Figure 6.31: 3D image of Site 8 on Senja. A debris field can be seen in towards the bottom of a steep slope and a cluster of debris is left behind further up the natural avalanche path.

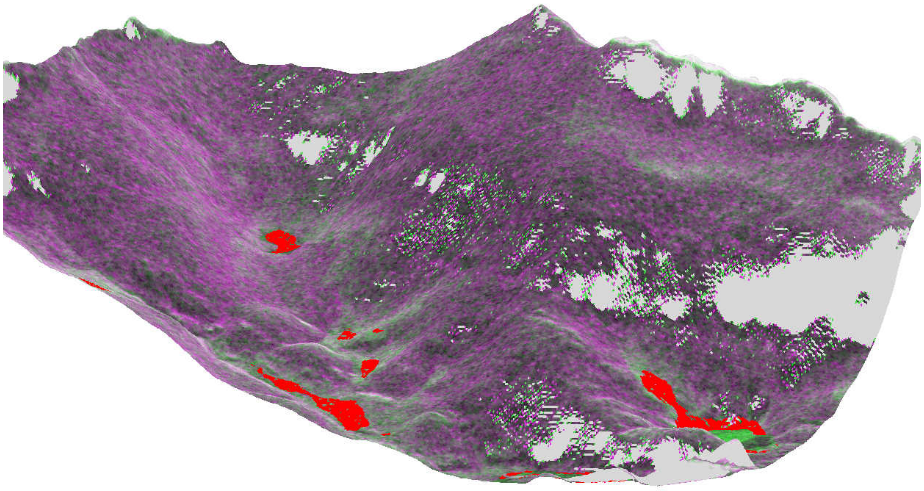

Figure 6.32: 3D image of Site 9 on Senja, the areas classified as avalanche can be in the end of the valley, a long debris field in the bottom left following a narrow valley and one debris field to the right.

in images, or taking several images in a time series and observe change in the backscatter from avalanche debris fields.

Another possible approach to remove areas with a higher backscatter could be to implement an upper and lower threshold that could mask away areas where the backscatter is stronger than from the avalanche debris fields. This is because the filtering algorithm presented here only mask away areas where the backscatter is to low to be included in avalanche mask created by the filtering algorithm.

The manually drawn masks should also be perfected by comparing the masks with aerial images or independent observations from other satellites such as high resolution optical satellites (SPOT-5 Worldview) and manual mapping of the debris field from the avalanche. A better mask for lakes and water can be applied that will allow for avalanche runouts on frozen lakes to be detected and not removed as they were in this thesis. A way of doing this is possibly by using water masks and shrinking them to such an extent that areas near the sea shore is included in the avalanche map.

Chapter 7

Conclusion

By using a filtering algorithm it was determined which speckle filter would have the highest accuracy when separate the higher backscatter inside the avalanche from the lower backscatter in the surrounding areas. This algorithm was used on 10 different subsets that have a high probability of containing avalanche debris fields or debris, and the algorithm found that the average filter had the best accuracy for classifying pixels, mean moving window size of 17x17 pixels, and a mean threshold of 1.52 was found to give the best performance (highest classification accuracy) for all 10 sites together. This allowed for the creation of avalanche masks, which are a mask that highlight areas where the difference in backscatter is higher than a given threshold. The avalanche masks are applied to a larger subset of each island, and several areas that are classified as avalanche debris fields are found in areas that have a very low probability of containing avalanche debris fields. These are other relative high backscatter areas, like frozen lakes that have a lower backscatter during the summer than in the winter, and clearing of roads during the winter creates hard packed snow near the roads and that have show similar relative backscatter as avalanches.

By using a Digital Elevation Model a slope mask is created. The slope mask is applied to remove all flat areas(lakes included)and areas that are too steep to contain avalanche debris fields.

Applying the filter data, seen in table 6.5, on the full images of Senja and Kattfjordeidet, and the slope masks and the geographic distortions mask from GSAR, creates an image where the avalanche debris fields for the entire image are clearly more visible. All the original sites are found and several new ones discovered and verified by creating 3D models. This is done to model the terrain around the avalanche debris field to make sure that it is not located somewhere that is improbable, such as in flat or very steep terrain.

More data would be needed to confirm the findings in this thesis. Avalanches found with this method should be confirmed by observers, in a short amount of time after the SAR image have been taken, to verify the presence of avalanche debris fields. Today the only avalanche that is verified and properly detectable with this method is the large avalanche in Tromdalen, Senja.

Future work should be done with the slope mask. The slope mask should mask out areas on ridges, flat areas to far away from slopes that are prune for avalanches and lakes, but not shorelines. This might be doable by using water masks to mask away waters and a slope mask like the one created here, but allowed to grow into flat areas where avalanche debris deposits are likely. Also verification of findings in this thesis should be prioritized to make sure that the avalanche debris fields are where the avalanche masks places them.

This method does, if verified, make a great tool for observing large areas and counting avalanches manually. This data can be used to improve avalanche runout models and for monitoring avalanche repeat cycle.

With new satellites, high resolution images might be delivered at a time higher rate than is possible today. Then this data could be calculated several times per week, and uploaded to websites like varsom.no. People who travel in the mountains could then check the website and observe where avalanches have been released. d It is worth noticing that the filtering algorithm compares the filtered avalanche mask with the manually drawn mask it was trained against. Also there is uncertainty about the extent of the avalanche debris fields. Only two of the sites containing avalanches have reported and verified avalanches in them, the other sites are visually identified by looking for relative high backscatter in terrain that are known to have a high probability for avalanches. These avalanches will have to be verified and mapped manually with GPS locations to make sure the algorithm is indeed working as intended.

The manually drawn masks that are drawn by the author and not verified by field studies, meaning there could be avalanche debris field outside of the masks created and used to find the best threshold, moving window size and filters. It would also have been better if optical data were available for verification of the avalanche debris fields. But no other data is available for these avalanches than what is used in this thesis so some presumptions had to be made, as that the relative high backscatter seen in the sites actually are avalanche debris field.

The very low threshold calculated in for Site 1 and 3 on Senja can be explained by a wet snow surrounding the avalanches and absorbing the microwaves and causing a general lower backscatter than the reference image has. But the difference in backscatter also show that it might be difficult to find one threshold that works uniformly for all areas. In this thesis an approximation was done by looking at the accuracy and deciding that its was good enough for all sites with a threshold of 1.5. But as can be seen, this cause some of areas with visible high backscatter to not be classified as avalanche. These areas might be of older avalanches with a weaker backscatter or just smaller avalanches.

With a time series of SAR images it might be possible to track avalanches over time, and observe how their age affects the backscatter. The algorithm developed in this thesis did manage to discover several new avalanche debris fields in the images over Senja and Kattfjordeidet, while maintaining the avalanche debris field selected for site 1 to 4 on Kattfjordeidet and 1 to 6 on Senja. Many false positives were removed by adding a slope mask to the avalanche mask and especially for Senja the final product were of reasonably high quality for both Senja and Kvaløya.

Bibliography

[Brattlien, 2013] Brattlien, K. (2013). NGI Report: Skredulykke Tromdalen Senja, Tirsdag 26.03.2013. `http://www.ngi.no/upload/Sn%f8skred/Ulykkesrapporter/ulykker_2013_26mars_Senja.pdf`. Accessed: 2013-11-15.

[Bühler et al., 2009] Bühler, Y., Hüni, A., Christen, M., Meister, R., and Kellenberger, T. (2009). Automated detection and mapping of avalanche deposits using airborne optical remote sensing data. *Cold Regions Science and Technology*, 57(2):99–106.

[Cheng et al., 2011] Cheng, Y., Li, X., Xu, Q., Garcia-Pineda, O., Andersen, O. B., and Pichel, W. G. (2011). Sar observation and model tracking of an oil spill event in coastal waters. *Marine pollution bulletin*, 62(2):350–363.

[Chuvieco et al., 2009] Chuvieco, E., Huete, A., et al. (2009). *Fundamentals of satellite remote sensing.* CRC Press Inc.

[Dent et al., 1998] Dent, J., Burrell, K., Schmidt, D., Louge, M., Adams, E., and Jazbutis, T. (1998). Density, velocity and friction measurements in a dry-snow avalanche. *Annals of Glaciology*, 26:247–252.

[Elachi and Van Zyl, 2006] Elachi, C. and Van Zyl, J. J. (2006). *Introduction to the physics and techniques of remote sensing*, volume 28. John Wiley & Sons.

[Frauenfelder et al., 2010] Frauenfelder, R., Kronholm, K., Solberg, R., Larsen, S. Ø., Salberg, A. B., Larsen, J. O., and Bjordal, H. (2010). Due avalrs: Remote-sensing derived avalanche inventory data for decision support and hind-cast after avalanche events.

[Frost et al., 1982] Frost, V. S., Stiles, J. A., Shanmugan, K. S., and Holtzman, J. (1982). A model for radar images and its application to adaptive digital filtering of multiplicative noise. *Pattern Analysis and Machine Intelligence, IEEE Transactions on*, (2):157–166.

[Gagnon and Jouan, 1997] Gagnon, L. and Jouan, A. (1997). Speckle filtering of sar images: a comparative study between complex-wavelet-based and standard filters. In *Optical Science, Engineering and Instrumentation'97*, pages 80–91. International Society for Optics and Photonics.

[Guneriussen et al., 1999] Guneriussen, T., Johnsen, H., and Lauknes, I. (1999). Snow cover mapping capabilities using radarsat standard mode data. In

Geoscience and Remote Sensing Symposium, 1999. IGARSS'99 Proceedings. IEEE 1999 International, volume 3, pages 1798–1800. IEEE.

[Huang and van Genderen, 1996] Huang, Y. and van Genderen, J. (1996). Evaluation of several speckle filtering techniques for ers-1&2 imagery. *International Archives of Photogrammetry and Remote Sensing*, 31:164–169.

[Imhoff, 1995] Imhoff, M. L. (1995). A theoretical analysis of the effect of forest structure on synthetic aperture radar backscatter and the remote sensing of biomass. *Geoscience and Remote Sensing, IEEE Transactions on*, 33(2):341–352.

[Kasischke et al., 2009] Kasischke, E. S., Bourgeau-Chavez, L. L., Rober, A. R., Wyatt, K. H., Waddington, J. M., and Turetsky, M. R. (2009). Effects of soil moisture and water depth on ers sar backscatter measurements from an alaskan wetland complex. *Remote Sensing of Environment*, 113(9):1868–1873.

[Koskinen et al., 2000] Koskinen, J., Pulliainen, J., and Hallikainen, M. (2000). Effect of snow wetness to c-band backscatter-a modeling approach. In *Geoscience and Remote Sensing Symposium, 2000. Proceedings. IGARSS 2000. IEEE 2000 International*, volume 4, pages 1754–1756. IEEE.

[Koskinen et al., 1997] Koskinen, J. T., Pulliainen, J. T., and Hallikainen, M. T. (1997). The use of ers-1 sar data in snow melt monitoring. *Geoscience and Remote Sensing, IEEE Transactions on*, 35(3):601–610.

[Landrø, 2002] Landrø, M. (2002). *Skredfare: snøskred, risiko, redning.* Featureforlaget.

[Larsen et al., 2010] Larsen, S. Ø., Salberg, A.-B., and Solberg, R. (2010). Automatic detection of avalanches in high-resolution optical satellite data results from the esa avalrs project s feasibility study on automated avalanche detection.

[Lauknes and Malnes, 2004] Lauknes, I. and Malnes, E. (2004). Automatical geocoding of sar products. In *Proc. Envisat ERS Symp.*

[Lee, 1983] Lee, J.-S. (1983). Digital image smoothing and the sigma filter. *Computer Vision, Graphics, and Image Processing*, 24(2):255–269.

[Magagi and Bernier, 2003] Magagi, R. and Bernier, M. (2003). Optimal conditions for wet snow detection using radarsat sar data. *Remote Sensing of Environment*, 84(2):221–233.

[Malnes et al., 2013] Malnes, E., Eckerstorfer, M., Larsen, Y., Frauenfelder, R., Jónsson, Á., Jaedicke, C., and Solbø, S. A. (2013). Remote sensing of avalanches in northern norway using synthetic aperture radar.

[Mansourpour et al., 2006] Mansourpour, M., Rajabi, M., and Blais, J. (2006). Effects and performance of speckle noise reduction filters on active radar and sar images. In *Proc. ISPRS*, pages 14–16.

[McClung and Schaerer, 2006] McClung, D. and Schaerer, P. A. (2006). *The avalanche handbook.* The Mountaineers Books.

[Moser and Serpico, 2006] Moser, G. and Serpico, S. B. (2006). Generalized minimum-error thresholding for unsupervised change detection from sar amplitude imagery. *Geoscience and Remote Sensing, IEEE Transactions on*, 44(10):2972–2982.

[Nagler and Rott, 2000] Nagler, T. and Rott, H. (2000). Retrieval of wet snow by means of multitemporal sar data. *Geoscience and Remote Sensing, IEEE Transactions on*, 38(2):754–765.

[Oh et al., 1992] Oh, Y., Sarabandi, K., and Ulaby, F. T. (1992). An empirical model and an inversion technique for radar scattering from bare soil surfaces. *Geoscience and Remote Sensing, IEEE Transactions on*, 30(2):370–381.

[Oliver and Quegan, 2004] Oliver, C. and Quegan, S. (2004). *Understanding synthetic aperture radar images*. SciTech Publishing.

[Pivot, 2012] Pivot, F. C. (2012). C-Band SAR Imagery for Snow-Cover Monitoring at Treeline, Churchill, Manitoba, Canada.

[Shi and Fung, 1994] Shi, J. Z. and Fung, K. B. (1994). A comparison of digital speckle filters. *Geoscience and Remote Sensing Symposium, 1994. IGARSS '94. Surface and Atmospheric Remote Sensing: Technologies, Data Analysis and Interpretation., International*, pages 2129–2133.

[Shirvany et al., 2012] Shirvany, R., Chabert, M., and Tourneret, J.-Y. (2012). Ship and oil-spill detection using the degree of polarization in linear and hybrid/compact dual-pol sar. *Selected Topics in Applied Earth Observations and Remote Sensing, IEEE Journal of*, 5(3):885–892.

[Snehmani et al., 2010] Snehmani, Venkataraman, G., Nigam, A., and Singh, G. (2010). Development of an inversion algorithm for dry snow density estimation and its application with envisat-asar dual co-polarization data. *Geocarto International*, 25(8):597–616.

[Storvold et al., 2005] Storvold, R., Malnes, E., and Lauknes, I. (2005). Using envisat asar wideswath data to retrieve snow covered area in mountainous regions. *EARSeL eProceedings*, 4(2):150–156.

[Susan Moran et al., 2000] Susan Moran, M., Hymer, D. C., Qi, J., and Sano, E. E. (2000). Soil moisture evaluation using multi-temporal synthetic aperture radar (sar) in semiarid rangeland. *Agricultural and Forest meteorology*, 105(1):69–80.

[Wakabayashi et al., 2013] Wakabayashi, H., Mori, Y., Nakamura, K., Osa, K., and Yang, C. (2013). A study on sea ice monitoring with sar data at lake saroma. In *Synthetic Aperture Radar (APSAR), 2013 Asia-Pacific Conference on*, pages 57–60. IEEE.

[Wiesmann et al., 2001] Wiesmann, A., Wegmuller, U., Honikel, M., Strozzi, T., and Werner, C. L. (2001). Potential and methodology of satellite based sar for hazard mapping. In *Geoscience and Remote Sensing Symposium, 2001. IGARSS'01. IEEE 2001 International*, volume 7, pages 3262–3264. IEEE.